

Scuola di Scienze  
Dipartimento di Fisica e Astronomia  
Corso di Laurea in Fisica

Measurement of effective cross section for  
luminosity measurements at the LHCb  
experiment using PLUME data

Relatore:

Dott. Fabio Ferrari

Presentata da:

Licia Mozzina

Correlatore:

Prof. Angelo Carbone

# Abstract

The Probe for LUminosity MEasurement (PLUME) detector is a luminometer installed in the LHCb experiment at the LHC, and the knowledge of its cross-section is essential to evaluate the instantaneous luminosity delivered to the LHCb experiment. The aim of this thesis is to present three different measurements of the PLUME detector effective cross-section, obtained with data collected during a van der Meer scan performed in November 2022.

The feature that distinguishes the three measurements is the definition of the proxy used to measure the luminosity. In order to obtain the following results for the cross-section ( $\sigma$ ), two innovative proxies, single photomultipliers (PMTs) rates and average of the collected ADC counts, have been studied in this thesis. A third proxy, the number of coincidences of particle hits in projective PLUME elementary detection modules, has been studied too in order to validate the analysis procedure with official PLUME cross-section determinations. The results obtained are

$$\begin{aligned} \text{Coincidences of PMTs hits} & \quad \sigma = (3.57 \pm 0.04) \text{ mb} \\ \text{Single PMT rates} & \quad \sigma = (29.63 \pm 0.03) \text{ mb} \\ \text{Average of ADC counts} & \quad \sigma = (10.06 \pm 0.01) \text{ mb} \end{aligned}$$

where the labels refer to the different proxies.

# Abstract

Il rivelatore Probe for LUminality MEasurement (PLUME) è un luminometro installato nell'esperimento LHCb al LHC, e la conoscenza della sua sezione d'urto è essenziale per calcolare la luminosità istantanea fornita all'esperimento LHCb. Lo scopo di questa tesi è presentare tre diverse misure della sezione d'urto efficace del rivelatore PLUME dell'esperimento LHCb, ottenute tramite dati raccolti con un van der Meer scan eseguito durante Novembre 2022.

La caratteristica che distingue le tre misure è la definizione della quantità utilizzata per misurare la luminosità. Per ottenere i seguenti valori della sezione d'urto ( $\sigma$ ), sono state studiate in questa tesi due quantità innovative, i ratei da singoli fotomoltiplicatori (PMTs) e le medie dei conteggi ADC raccolti. Una terza quantità, il numero di coincidenze di passaggi di particelle in moduli elementari successivi del rivelatore PLUME, è stata studiata per confrontare la procedura di analisi con le misure ufficiali di sezione d'urto di PLUME. I risultati ottenuti sono

$$\begin{aligned} \text{Coincidenze di passaggio nei PMT} & \quad \sigma = (3.57 \pm 0.04) \text{ mb} \\ \text{Ratei da singoli PMT} & \quad \sigma = (29.63 \pm 0.03) \text{ mb} \\ \text{Media del conteggio di ADC} & \quad \sigma = (10.06 \pm 0.01) \text{ mb} \end{aligned}$$

dove le didascalie indicano le diverse quantità analizzate.

# Contents

<b>Introduction</b>	<b>4</b>
<b>1 Luminosity in particle physics</b>	<b>5</b>
1.1 Fixed target experiments . . . . .	5
1.2 Colliding beams experiments . . . . .	5
1.3 Van der Meer scan . . . . .	10
<b>2 The LHCb experiment</b>	<b>11</b>
2.1 The Large Hadron Collider . . . . .	11
2.2 The LHCb detector . . . . .	12
2.3 Tracking System . . . . .	13
2.3.1 VELO . . . . .	14
2.3.2 Upstream Tracker . . . . .	14
2.3.3 SciFi Tracker . . . . .	15
2.3.4 Magnet . . . . .	15
2.4 Particle identification system . . . . .	16
2.4.1 RICH detectors . . . . .	16
2.4.2 Calorimeters . . . . .	17
2.4.3 Muon Detectors . . . . .	18
<b>3 The PLUME detector</b>	<b>19</b>
3.1 PLUME detector layout . . . . .	19
3.2 Elementary detection module . . . . .	19
3.3 Photomultiplier R760 . . . . .	21
3.4 Quartz radiator . . . . .	21
<b>4 Measurements of PLUME effective cross-section</b>	<b>22</b>
4.1 Data Sample . . . . .	22
4.2 Data Analysis . . . . .	24
4.2.1 The LogZero Method . . . . .	24
4.2.2 Maximum-likelihood fit for cross-section measurements . . . . .	26
4.2.3 Computation of cross-section uncertainty . . . . .	33
<b>Conclusions</b>	<b>36</b>
<b>A The maximum likelihood method</b>	<b>38</b>

# Introduction

The PLUME detector is a luminometer installed at the LHCb experiment of the CERN Large Hadron Collider. It has been installed before the start of Run 3 in 2022. This run is characterized by a remarkable increase in the instantaneous luminosity delivered to LHCb, approximately five times greater than previous runs. The PLUME detector serves the purpose of instantaneous luminosity monitoring, which is fundamental for optimal and safe working conditions of the whole experiment.

Until now, the PLUME detector has measured luminosity requiring signals above threshold in a pair of projective elementary detection modules (PMTs). This thesis will report two additional proxies for luminosity measurements: single PMT rates, *i.e.* single PMT signals over threshold, and the average of ADC counts. These proxies are interesting to study since they are affected by different experimental biases with respect to the official proxy. Thus, their employment could help in reducing the uncertainty on the luminosity determination of the LHCb experiment.

This thesis is organised as follows. The first chapter explains the concept of luminosity in particle physics, specifically in colliding beams experiments. It also describes the van der Meer scan and its mathematical basis. A brief overview of the LHCb experiment will be given in the second chapter, alongside a description of its detectors main features. The third chapter will show the PLUME detector layout and the structure of its elementary detection modules. Finally, the last chapter will describe the data sample used to perform the analysis and the experimental techniques adopted to obtain the cross-section. In this chapter there will also be a description of the two methods used to compute the cross-section uncertainty: the classical propagation of uncertainty and the computation of uncertainty via a toy Monte Carlo generation.

# Chapter 1

## Luminosity in particle physics

In particle physics at accelerators one of the most important parameters is the number of useful interactions (events) that are produced. This quantity is called luminosity and represents the proportionality factor between the number of events per second  $d\mu/dt$  and the cross-section  $\sigma$  of a process:

$$\frac{d\mu}{dt} = \mathcal{L}\sigma. \quad (1.1)$$

It can be easily seen that  $\mathcal{L}$  is measured in  $cm^{-2} s^{-1}$ . Luminosity values greatly depend on the experiment's type and geometry. Two particular cases will be shown in the following sections.

### 1.1 Fixed target experiments

The easiest way to compute  $\mathcal{L}$  is to consider a fixed target, characterized by its density  $\rho_T$  and its length  $l$  [1]. A colliding beam with flux  $\Phi$  impinges on the target: if the latter is homogeneous and larger than the former, the beam distribution can be ignored. The situation is sketched in Fig. 1.1. The luminosity can be found from

$$\mathcal{L}_{FT} = \Phi\rho_T l, \quad (1.2)$$

while the interaction rate is defined as

$$\frac{d\mu}{dt} = \Phi\rho_T l \cdot \sigma = \mathcal{L}_{FT} \cdot \sigma. \quad (1.3)$$

### 1.2 Colliding beams experiments

Finding an analytical expression for  $\mathcal{L}$  becomes trickier when we consider two colliding beams. In this case, the beams are both targets and “incoming” beams. This dissertation will address bunched beams, as those produced at the CERN Large Hadron Collider (LHC) and shown in Fig. 1.2.

Unlike the previous case, the beam density distribution is now extremely important, leading us to compute an overlap integral on multiple variables. The overlap integral is proportional to luminosity.

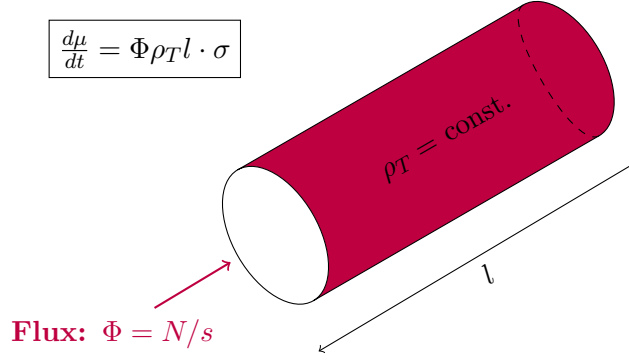


**Figure 1.1:** Sketch of a fixed target experiment: an incident beam of flux  $\Phi$  impinges on a target of length  $l$  and density  $\rho_T$ .

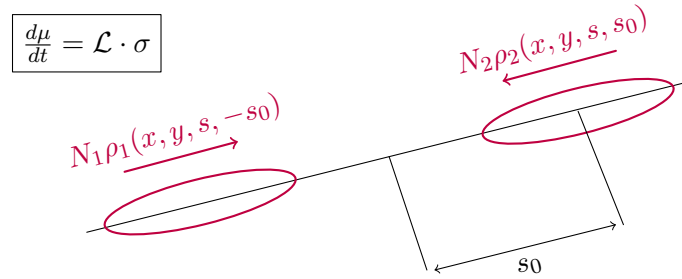


**Figure 1.2:** Sketch of two colliding bunches. The relevant quantities are described in the text.

The resulting integration is therefore performed not only on the transversal coordinates  $(x, y)$ , but also, since the bunches are moving towards each other, on the longitudinal one  $(s)$  and on time. The distance between each beam and the central collision point  $s_0 = c \cdot t$  serves as the time variable. We assume that the collision takes place at  $s_0 = 0$ . Then the luminosity can be expressed as

$$\mathcal{L} = K \cdot \iiint \rho_1(x, y, s, -s_0) \rho_2(x, y, s, s_0) dx dy ds ds_0, \quad (1.4)$$

where  $\rho_1(x, y, s, -s_0)$  and  $\rho_2(x, y, s, s_0)$  are the time-dependent beam density distribution functions. The quantity  $K$  is a kinematic factor that is equal to

$$K = \sqrt{(\vec{v}_1 - \vec{v}_2)^2 - \frac{(\vec{v}_1 \times \vec{v}_2)^2}{c^2}}. \quad (1.5)$$

The case  $K = 2$  corresponds to an head-on collision, *i.e.*  $\vec{v}_1 = -\vec{v}_2$ , of bunches travelling almost at the speed of light, as we will assume in the following. We will also assume that all densities are uncorrelated in all planes.

Furthermore, to compute  $\mathcal{L}$  in the present case of colliding bunched beams we will need to consider the make up of bunches, which are composed of particles. At every bunch-crossing, respectively  $N_1$  and  $N_2$  particles per beam may interact. To get the total

number of bunch-crossings in each beam revolution period, it is sufficient to multiply the revolution frequency  $f$  by the number of bunches per beam  $N_b$ . In this way, as seen in Equation 1.1, the strict proportionality between the luminosity and the number of events per second, *i. e.* the interaction rate, is explicated in what follows:

$$L = 2N_1N_2fN_b \iiint \rho_{1x}(x)\rho_{1y}(y)\rho_{1s}(s-s_0)\rho_{2x}(x)\rho_{2y}(y)\rho_{2s}(s+s_0)dx dy ds ds_0. \quad (1.6)$$

Theoretically, one should know all distributions of the variables involved, but often it is reasonable to assume that the bunches follow a Gaussian profile. Thus, the luminosity is determined by the overlap of the core of the distribution and it is safe to assume that the tails give no contribution.

For coordinates  $z = x, y$  the density distribution can be expressed as

$$\rho_z(z) = \frac{1}{\sigma_z\sqrt{2\pi}} \exp\left(-\frac{z^2}{2\sigma_z^2}\right), \quad (1.7)$$

while for the parameter  $s \pm s_0$

$$\rho_s(s \pm s_0) = \frac{1}{\sigma_s\sqrt{2\pi}} \exp\left(-\frac{(s \pm s_0)^2}{2\sigma_s^2}\right). \quad (1.8)$$

Moreover, equal beams are assumed, *i. e.*  $\sigma_{1x} = \sigma_{2x}$ ,  $\sigma_{1y} = \sigma_{2y}$  and  $\sigma_{1s} = \sigma_{2s}$ . Substituting these expressions in Equation 1.6, we find that

$$L = \frac{2N_1N_2fN_b}{(\sqrt{2\pi})^6\sigma_s^2\sigma_x^2\sigma_y^2} \iiint \int e^{-\frac{x^2}{\sigma_x^2}} e^{-\frac{y^2}{\sigma_y^2}} e^{-\frac{s^2}{\sigma_s^2}} e^{-\frac{s_0^2}{\sigma_s^2}} dx dy ds ds_0. \quad (1.9)$$

We can then integrate over  $s$  and  $s_0$ , using the well known formula

$$\int_{-\infty}^{+\infty} e^{-at^2} dt = \sqrt{\pi/a}. \quad (1.10)$$

The intermediate result is

$$L = \frac{2N_1N_2fN_b}{8(\sqrt{\pi})^4\sigma_x^2\sigma_y^2} \iint e^{-\frac{x^2}{\sigma_x^2}} e^{-\frac{y^2}{\sigma_y^2}} dx dy. \quad (1.11)$$

By integrating over  $x$  and  $y$ , we finally obtain

$$\mathcal{L} = \frac{N_1N_2fN_b}{4\pi\sigma_x\sigma_y}. \quad (1.12)$$

At the LHC, the beams collide perfectly head-on in the ATLAS and CMS experiments, while at the LHCb experiment the collision is not perfectly head-on, but with both a crossing angle  $\phi$  and a small transversal offset with respect to the beams reference orbits. This is necessary to keep the instantaneous luminosity delivered to the LHCb experiment down to a manageable level. This crossing angle and the offset are continuously adjusted to keep the instantaneous luminosity roughly constant during an LHC fill. This procedure

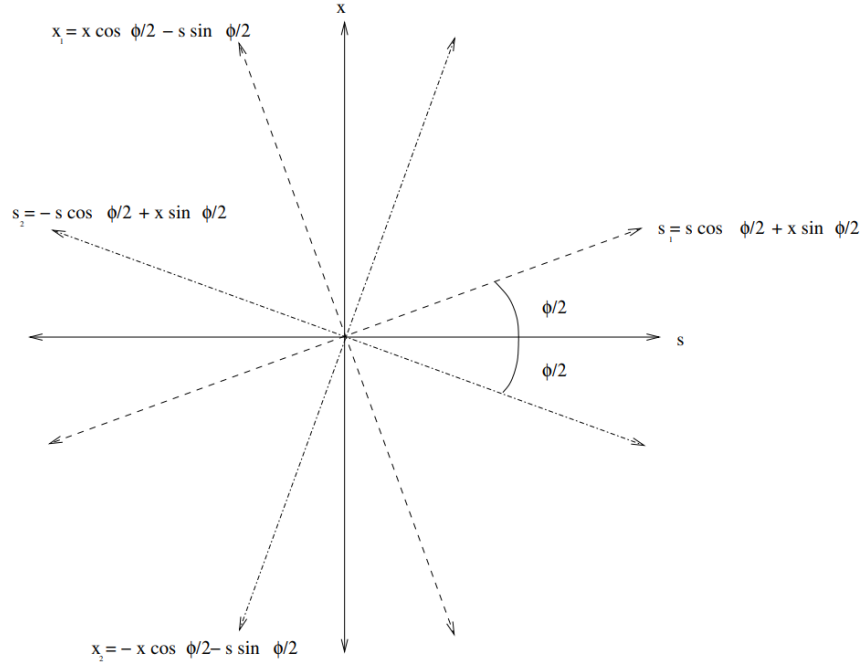


**Figure 1.3:** Transformation of coordinates.

is called luminosity levelling and it is of fundamental importance to ensure a safe and optimal working point for the LHCb experiment.

To study this case, for the sake of symmetry, the total crossing angle is made up by two rotations  $\phi/2$  and  $-\phi/2$ . The coordinates undergo the following transformation:

$$x_1 = d_1 + x \cos \frac{\phi}{2} - s \sin \frac{\phi}{2}, \quad s_1 = s \cos \frac{\phi}{2} - s \sin \frac{\phi}{2}, \quad (1.13)$$

$$x_2 = d_2 + x \cos \frac{\phi}{2} + s \sin \frac{\phi}{2}, \quad s_2 = s \cos \frac{\phi}{2} + s \sin \frac{\phi}{2}. \quad (1.14)$$

With these considerations, the expression for the luminosity reported in Eq. (1.12) becomes

$$\mathcal{L} = \frac{N_1 N_2 f N_b}{4\pi\sigma_x\sigma_y} \cdot W \cdot e^{\frac{B^2}{A}} \cdot S. \quad (1.15)$$

where  $W$ ,  $e^{\frac{B^2}{A}}$ , and  $S$  are correction factors. More specifically,

$$W = e^{\frac{1}{4\sigma_x^2} (d_2 - d_1)^2}. \quad (1.16)$$

represents the reduction in luminosity due to the beam offsets, and

$$S = \frac{1}{\sqrt{(1 + \frac{\sigma_s}{\sigma_x} \tan \frac{\phi}{2})^2}} \approx \frac{1}{\sqrt{(1 + \frac{\sigma_s \phi}{\sigma_x})^2}}. \quad (1.17)$$

represents the reduction in luminosity due to the crossing angles.

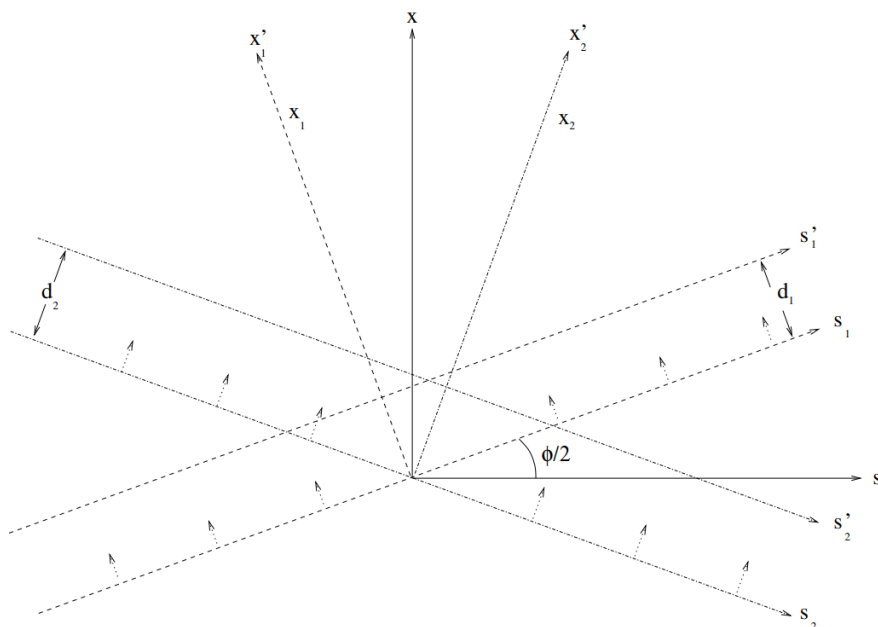


**Figure 1.4:** Transformation of coordinates with displacements.

Finally,  $e^{\frac{B^2}{A}}$  is only present when a crossing angle and an offset are present simultaneously. The values of the parameters  $A$  and  $B$  entering this factor are

$$A = \frac{\sin^2 \frac{\phi}{2}}{\sigma_x^2} + \frac{\cos^2 \frac{\phi}{2}}{\sigma_s^2}, \quad B = \frac{(d_2 - d_1) \sin(\frac{\phi}{2})}{2\sigma_x^2}. \quad (1.18)$$

We are not only interested in the maximum luminosity and consequently the instantaneous number of interactions per second, but also in the integrated luminosity

$$\mathcal{L}_{int} = \int_0^T \mathcal{L}(t') dt'. \quad (1.19)$$

since it is directly linked to the number of observed events for a given process with cross-section  $\sigma$  by

$$\mathcal{L}_{int} \cdot \sigma = \mu. \quad (1.20)$$

As shown throughout this section, in order to measure the luminosity one needs to know the effective cross-section of the detector exploited to perform such measurement. By effective we mean that this cross-section is not only geometrical in nature, but includes also detector related effects, *e.g.* the threshold chosen for a given proxy. The effective cross-section can be determined in a non-destructive way in a collider via the van der Meer scan, as described in the next section.

### 1.3 Van der Meer scan

At a hadron collider, an absolute value of a detector cross-section can be obtained via the *van der Meer scan* [2]. This procedure separates two colliding bunches, respectively with  $N_1$  and  $N_2$  particles, in the transverse plane.

Due to the separations  $\Delta x$ ,  $\Delta y$  the instantaneous luminosity is reduced as we have seen in Equation 1.15, and the same reduction affects the number of observed interactions.

We can compute  $\mu$  rescaled by  $N_1 N_2$ :

$$\frac{\mu(\Delta x, \Delta y)}{N_1 N_2} = \sigma \frac{\mathcal{L}_{int}}{N_1 N_2} = \sigma \iint \rho_1(x_2 + \Delta x, y_2 + \Delta y) \rho_2(x_2, y_2) dx_2 dy_2. \quad (1.21)$$

where  $\rho_1$ ,  $\rho_2$  are the normalized transverse particle density functions of the two beams. If we perform the integral in Equation 1.21 over  $\Delta x$ ,  $\Delta y$  we get

$$\iiint \rho_1(x_2 + \Delta x, y_2 + \Delta y) \rho_2(x_2, y_2) dx_2 dy_2 d\Delta x d\Delta y = 1. \quad (1.22)$$

This result can be easily proven by changing  $x_2 + \Delta x$ ,  $y_2 + \Delta y$  with  $x_1$ ,  $y_1$ : in this way the integrals decouple and reduce to unity by definition.

From Equation 1.21, we find the van der Meer formula

$$\sigma = \iint \frac{\mu(\Delta x, \Delta y)}{N_1 N_2} d\Delta x d\Delta y. \quad (1.23)$$

We can define the ratio  $\mu(\Delta x, \Delta y)/N_1 N_2$  as the specific number of interactions  $\mu_{sp}$ : this will allow the following formula to be valid in cases such as the decrease of beam current with time, as long as  $\mu(\Delta x, \Delta y)$ ,  $N_1 N_2$  vary proportionally and  $\rho_1$ ,  $\rho_2$  remain constant.

Assuming that the beam densities can be factorised into their  $x$  and  $y$  parts, consequently  $\mu_{sp}(\Delta x, \Delta y)$  can be factorised, thus leading to

$$\begin{aligned} \sigma &= \iint \mu_{sp}(\Delta x, \Delta y) d\Delta x d\Delta y = \int \mu_{sp}^x(\Delta x) d\Delta x \int \mu_{sp}^y(\Delta y) d\Delta y \frac{\mu_{sp}^x(\Delta x_0) \mu_{sp}^y(\Delta y_0)}{\mu_{sp}^x(\Delta x_0) \mu_{sp}^y(\Delta y_0)} \\ &= \frac{\int \mu_{sp}(\Delta x, \Delta y_0) d\Delta x \int \mu_{sp}(\Delta x_0, \Delta y) d\Delta y}{\mu_{sp}(\Delta x_0, \Delta y_0)}. \end{aligned} \quad (1.24)$$

The integrals at the numerator can be measured by means of two one dimensional van der Meer scans over  $\Delta x$  (respectively  $\Delta y$ ) with fixed  $\Delta y_0$  ( $\Delta x_0$ ). This formula is valid for every  $(\Delta x_0, \Delta y_0)$ , though it is convenient to choose  $(\Delta x_0, \Delta y_0)$  not too far from the point of maximum luminosity in order to collect enough interaction statistics.

The whole procedure relies on the  $x - y$  factorizability of  $\mu$ , that at LHC is good but not perfect: the accuracy can be improved by performing two dimensional scans over the central region, as it has been done since 2017. These scans are fast but allow the evaluation of  $\sim 90\%$  of the integral. Furthermore, at the LHC the scan is performed stepwise, so the function  $\mu_{sp}(\Delta x, \Delta y)$  is measured only in a predefined set of discrete points and then an analytical function is fit to the data to get the final integral.

# Chapter 2

## The LHCb experiment

The LHCb experiment is one of the four main experiments at the Large Hadron Collider (LHC) at CERN. In this chapter a brief description of its sub-detector systems will be provided.

### 2.1 The Large Hadron Collider

The Large Hadron Collider [3] is the world's largest particle accelerator. It is located 100 m underground, across the border between France and Switzerland, in the 26.7 km tunnel that once hosted LEP, the electron-positron collider. The LHC is designed to collide proton beams with a centre-of-mass energy up to 14 TeV and to reach an instantaneous luminosity of  $10^{34} \text{ cm}^{-2}\text{s}^{-1}$ .

The LHC is the final stage of a long chain of accelerator systems, receiving proton beams with an energy of 450 GeV from the Super Proton Synchrotron (SPS). The protons travel in two rings in two opposite directions, and they cross at four interaction points (IP), where the 4 main experiments are placed (ALICE, ATLAS, CMS, LHCb). A complete overview of LHC can be seen in Figure 2.1.

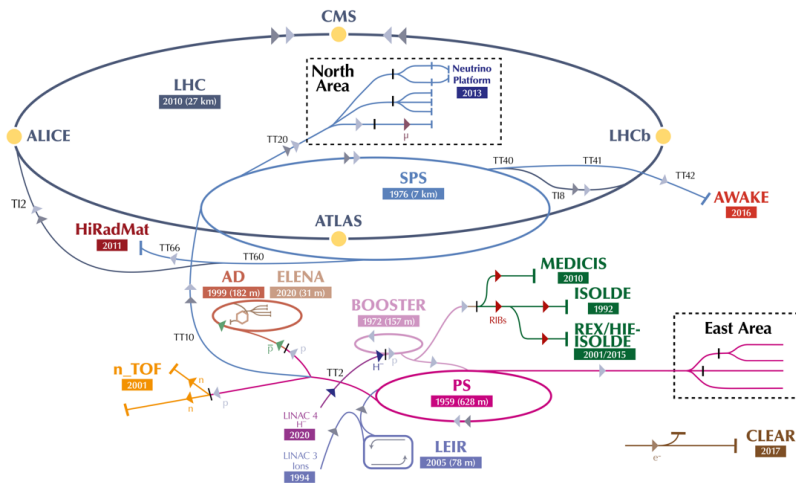


Figure 2.1: The CERN complex of accelerators [4].

The protons are grouped in bunches: from 2010 to 2018, during the operation in Run 1 (centre-of-mass energy  $\sqrt{s} = 7$  and 8 TeV in 2011 and 2012, respectively) and Run 2 ( $\sqrt{s} = 13$  TeV), there was a maximum of 2556 bunches, each with a population of  $1.12 \times 10^{11}$  protons. The bunches collided every 50 ns until 2016, and every 25 ns since then [5]. In Run 3, that started in 2022, a centre-of mass-energy of 13.6 TeV has been reached, with a consequent increase in luminosity and number of visible interactions per bunch crossing ( $\mu$ ).

## 2.2 The LHCb detector

The LHCb experiment is one of the four main experiments on the LHC circumference, operating at LHC interaction point IP8. Its primary goal is to look for indirect evidence of new physics in  $CP$  violation and rare decays of beauty and charm hadrons [6]. During Run 1 and Run 2, it operated at a smaller instantaneous luminosity ( $4 \times 10^{32} \text{ cm}^{-2}\text{s}^{-1}$ ) compared to other experiments, in order to keep pile-up at a sustainable level and to reduce radiation damage to the components of the detector. The LHCb detector has undergone a major upgrade at the end of Run 2, since all the sub-detectors have been almost completely renewed [7]. Since the start of Run 3 in 2022, the LHCb detector has been designed to operate at an instantaneous luminosity equal to  $2 \times 10^{33} \text{ cm}^{-2}\text{s}^{-1}$ , five times larger than before, and to collect events at the LHC crossing rate of 40 MHz. The events are then discriminated by a software trigger reconstructing in real time all events at the visible interaction rate of  $\sim 30$  MHz.

The LHCb detector is a single-arm forward spectrometer, designed with a forward angular coverage from approximately 10 mrad to 300 (250) mrad in the horizontal (vertical) plane that corresponds to a pseudorapidity acceptance region  $2 < \eta < 5$ <sup>1</sup>. The choice of the detector geometry is justified by the fact that at high energies both the  $b\bar{b}$  and  $c\bar{c}$  pairs originating from  $pp$  collisions are predominantly produced in the same forward or backward cone with respect to the beam direction. A cross-sectional lateral view of the spectrometer is displayed in Figure 2.2. The principal features characterising the LHCb detector are:

- an efficient, robust and flexible trigger that allows to cope with the harsh hadronic environment and that is sensitive to many different final states;
- a high precision detector (VELO) able to reconstruct interaction and decay vertexes of beauty and charm hadrons: its tracks are combined with the ones reconstructed by other two detectors (UT and SciFi);
- a good particle identification performance made possible by two RICH detectors, an electromagnetic (ECAL) and an hadronic (HCAL) calorimeter and muon detectors: this is fundamental to reconstruct the different final states originating from beauty and charm decays;
- a data acquisition system with high bandwidth and powerful online data processing capability, to optimize data taking.

---

<sup>1</sup> $\eta \equiv -\ln(\tan \frac{\theta}{2})$  where  $\theta$  is the angle between the particle three-momentum  $\mathbf{p}$  and the positive direction of the beam axis.

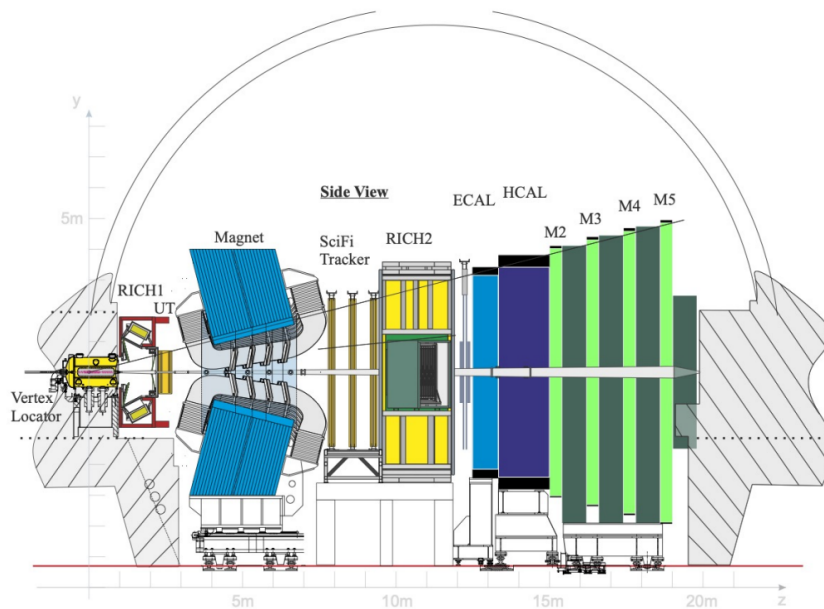


**Figure 2.2:** The LHCb detector [7].

The following brief description of the upgraded LHCb components for Run 3 will be divided into two areas:

- Tracking system, consisting of the VERtEX LOcator (VELO), surrounding the interaction point, the Upstream Tracker (UT) and the scintillating fibre tracker (SciFi). The silicon-strip UT lies upstream the magnet, while the three scintillating fibre tracker stations lie downstream of it. The latter replace both the straw-tube Outer Tracker and silicon-strip Inner Tracker used in Run 1 and Run 2.
- Particle identification system (PID), including two Ring Imaging CHerenkov detectors (RICH 1 and RICH 2), positioned upstream and downstream of the magnet, a *shashlik*-type electromagnetic calorimeter (ECAL), an iron-scintillator tile sampling hadronic calorimeter (HCAL) and four muon stations (M2-M5) interleaved with iron shielding.

During Run 1 and Run 2 the real-time luminosity measurement was based on information available in the hardware level-0 trigger (L0). In the upgraded experiment, a dedicated luminosity sub-detector, the Probe for LUminosity MEasurement (PLUME), has been installed. Luminosity monitoring is essential since deviations from the target value may affect the quality of collected data and could also damage the detector. A more detailed description of the PLUME apparatus will be provided in the next section (chapter 3).

## 2.3 Tracking System

The tracking system is dedicated to the identification of interaction vertices and the reconstruction of charged particle tracks traversing the detector. The reconstruction is

made possible by joining the hits deposited in the tracking devices and by measuring the track momentum, since the particle trajectory curves in the presence of a magnetic field.

### 2.3.1 VELO

A distinguishing characteristic of  $b$ - and  $c$ -hadron decays is the presence of a secondary vertex close to the interaction point. The Vertex LOcator (VELO) performs precise measurements of track coordinates close to the interaction region, that allow to identify the interaction vertices, the displaced secondary vertices and to measure their distance.

The VELO has been redesigned for compatibility with the higher luminosity and the trigger-less 40 MHz required readout. The new core technology of the VELO is pixelated hybrid silicon detectors, arranged into 52 identical modules and cooled by a silicon microchannel cooler. The modules are populated with pixelated ASICs (application specific integrated circuits) and are arranged perpendicular to the beam line. Their distribution covers the full pseudorapidity acceptance of LHCb ( $2 < \eta < 5$ ).

The modules are made up by two movable halves, Side A and Side C, nominally spaced at 25 mm. Side A modules are displaced in  $z$  by +12.5 mm relative to the Side C ones to ensure their overlapping when closed in order to provide a complete azimuthal coverage. As Figure 2.3 (right) displays, the rectangular pixels are arranged in a rotated ‘L’ shape.

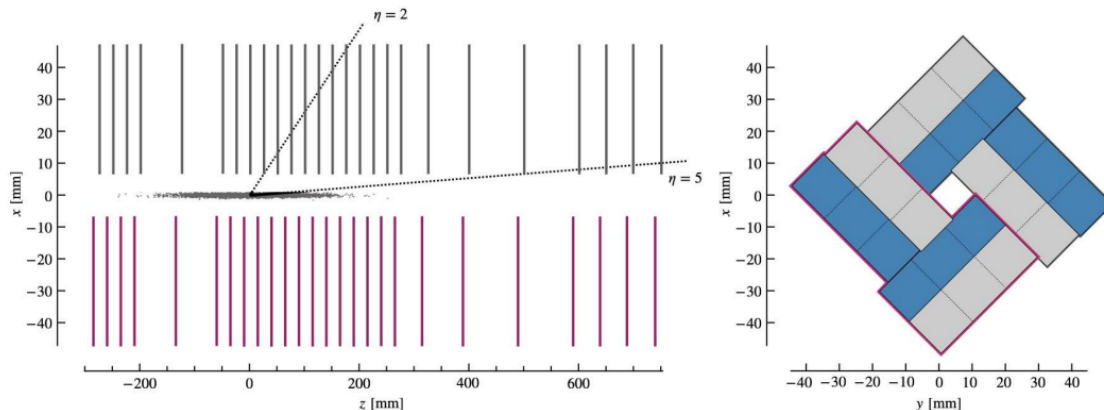


**Figure 2.3:** Left: schematic top view of the  $z-x$  plane at  $y=0$  (left) with an illustration of the  $z$ -extent of the luminous region and the nominal LHCb pseudorapidity acceptance,  $2 < \eta < 5$ . Right: sketch showing the nominal layout of the ASICs around the  $z$  axis in the closed VELO configuration. Half the ASICs are placed on the upstream module face (grey) and half on the downstream face (blue). The modules on the Side C are highlighted in purple on both sketches [7].

### 2.3.2 Upstream Tracker

The Upstream Tracker is positioned between RICH1 and the LHCb dipole magnet. It replaces the Tracking Turicensis used during Run 1 and Run 2. The UT contributes

to charged-particle tracking and to the first processing algorithm in the software trigger. The UT hits are combined with the VELO tracks and a first measurement of the track momentum  $p$  is obtained exploiting the magnetic field between the interaction region and the UT. It also provides measurements for particles decaying after the VELO.

The UT is composed of four planes of silicon detectors (Figure 2.4) organised in two stations. In the first and the fourth plane the silicon strips are parallel to the vertical plane, while in the second and the third ones they are tilted respectively by  $+5^\circ$  and  $-5^\circ$ , in order to improve the precision of track reconstruction.

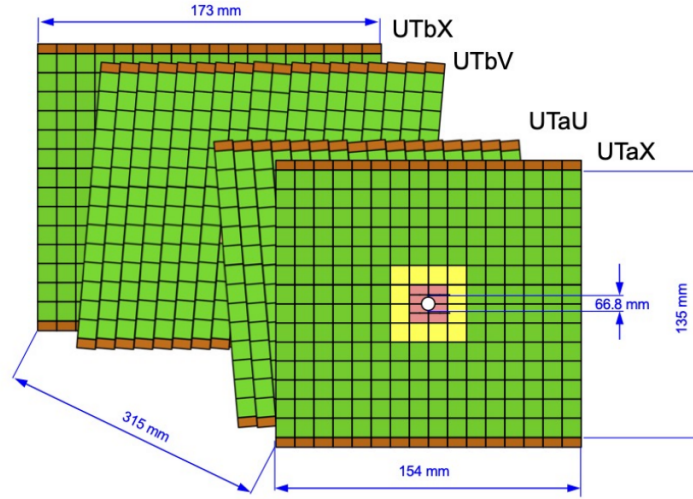


**Figure 2.4:** Drawing of the four UT silicon planes with indicative dimensions. Different colours designate different types of sensors: Type-A (green), Type-B (yellow), Type-C and Type-D (pink) [7].

### 2.3.3 SciFi Tracker

Like the UT, the Scintillating Fibre tracker is used for charged-particle tracking and momentum measurement. It is located between the magnet and RICH2. The SciFi technology is based on  $250 \mu\text{m}$  diameter plastic scintillating fibres arranged in multilayered fibre mats, for a total of 12 detection planes arranged in three stations (T1, T2, T3) with four layers each (Figure 2.5). In the first and the fourth layer the fibres are oriented vertically, and they serve the purpose of determining the curves in the charge particles trajectories due to the magnetic field. In the second and the third ones they are tilted respectively by  $+5^\circ$  and  $-5^\circ$ , in order to reconstruct the vertical position of the track hit.

### 2.3.4 Magnet

The momentum of charged particles is inferred from measuring their trajectory curvature in a magnetic field. The LHCb magnet has been maintained unchanged with respect to Run 1 and Run 2: it is a warm, *i.e.* non superconductive, dipole magnet, located

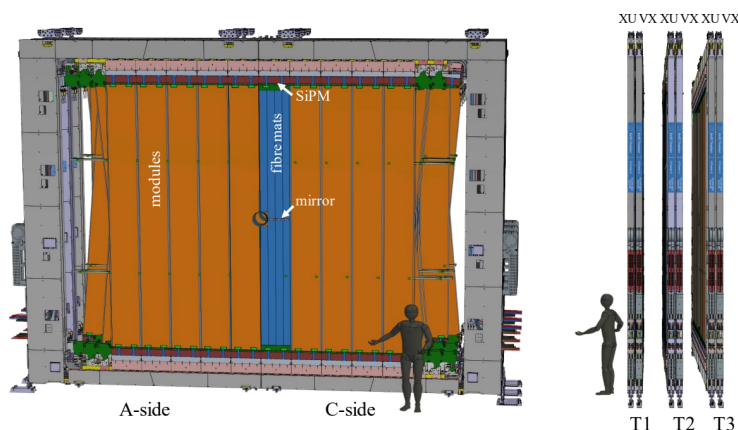


**Figure 2.5:** Front and side views of the 3D model of the SciFi Tracker detector [7].

between the UT and the SciFi tracker. The magnet is made up by two trapezoidal aluminium coils weighing 54 tonnes, that are slightly inclined with respect to the  $z$  axis as to follow the profile of the detector acceptance. The magnet provides a vertical magnetic field with a bending power of  $\sim 4$  Tm.

An important feature of the LHCb magnet is the possibility of reversing its polarity during data acquisition, which allows the control of the left-right asymmetries introduced by the detector.

## 2.4 Particle identification system

For a correct invariant mass reconstruction of  $b$ - and  $c$ -hadron decays, a particle identification system is essential to determine the nature of the final products of the decay. In the following, a brief description of the particle identification detectors installed in the LHCb experiment will be provided.

### 2.4.1 RICH detectors

The LHCb detector exploits two RICH detectors to discriminate between charged pions, kaons and protons in the 2.6-100 GeV/ $c$  momentum range. The overall layout and concept of the RICH systems, visible in Figure 2.6, remains unchanged with respect to Run 1 and 2, although some changes were made in order to cope with the increased instantaneous luminosity in operating conditions. Both devices are based on the detection of Cherenkov radiation which is emitted by a charged particle travelling in a medium at a higher velocity than that of light in the same medium. The relation between the Cherenkov photon emission angle  $\theta_c$  and the refraction index  $n$  of the radiator is

$$\cos(\theta_c) = \frac{1}{\beta n}, \quad (2.1)$$

where  $\beta = v/c$  is the ratio between the particle velocity and the speed of light in vacuum. Therefore, by measuring  $\theta_c$  the particle velocity is obtained, and this allows to infer its

invariant mass. For the Cherenkov light emission to occur,  $\beta$  has to exceed the threshold value  $\beta_{th} = 1/n$ . Each radiator has a maximum emission angle  $\theta_c^{max} = \arccos(1/n)$  when  $v = c$ . When particles approach the speed of light, their Cherenkov angle saturates to  $\theta_c^{max}$ , making it vital to have different radiators in order to discriminate particles in a wide range of momenta.

The RICH1 detector is placed immediately after the VELO and covers the low momentum range  $\sim 2.6\text{--}60$  GeV/c using a  $\text{C}_4\text{F}_{10}$  radiator; the RICH2 system is installed after the tracking stations and covers the high momentum range from  $\sim 15$  GeV/c to 100 GeV/c using a  $\text{CF}_4$  radiator. In order to readout the detectors at a 40 MHz rate, the full photon detection chain was replaced in both detectors, since the previous one was limited to a 1MHz output rate.

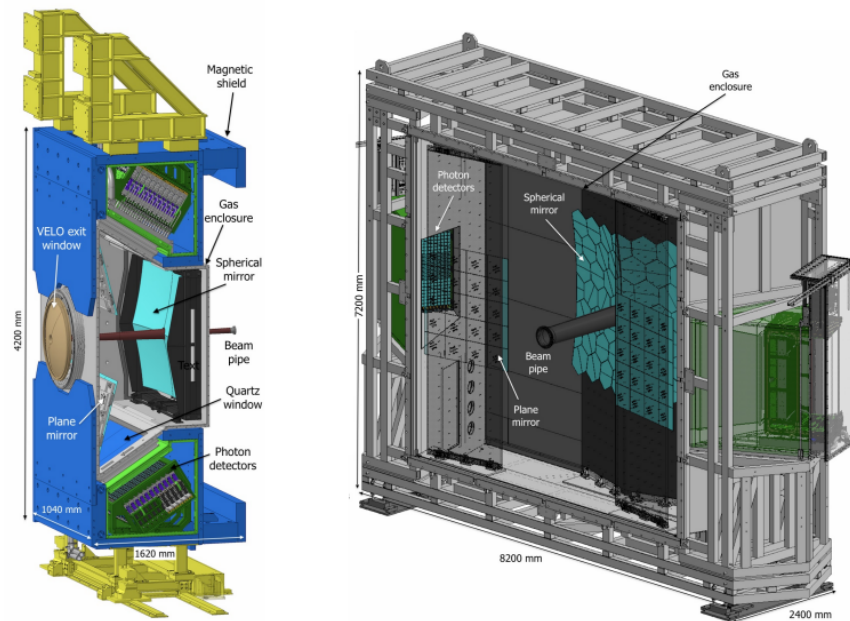


**Figure 2.6:** Schematic view of the (left) RICH1 and (right) RICH2 detectors [7].

## 2.4.2 Calorimeters

The LHCb calorimeter system is composed of an electromagnetic calorimeter followed by a hadronic calorimeter. Their purpose is to identify electrons and pions with an optimal energy resolution. The calorimeters layout is the same as Run 1 and Run 2.

Since hit densities are different across the calorimeter surface, the ECAL is segmented in three different regions (inner, middle and outer with respect to the beam pipe) while HCAL is segmented in two regions (Figure 2.7). The regions are in turn segmented in cells, which are optimised to provide uniform measurements of the transverse energy  $E_T = E_c \sin \theta$ , where  $E_c$  is the energy measured by a cell and  $\theta$  is the angle between the vector pointing to the centre of the cell from the interaction point. The ECAL cells have a *shashlik* structure, with alternated scintillator and lead layers, while HCAL deploys

staggered iron and plastic scintillator tiles mounted in parallel to the beam axis. Both calorimeters share the same basic detection principle: scintillation light from plastic scintillator modules is transmitted to photomultipliers (the same type is used for ECAL and HCAL) by fibres.

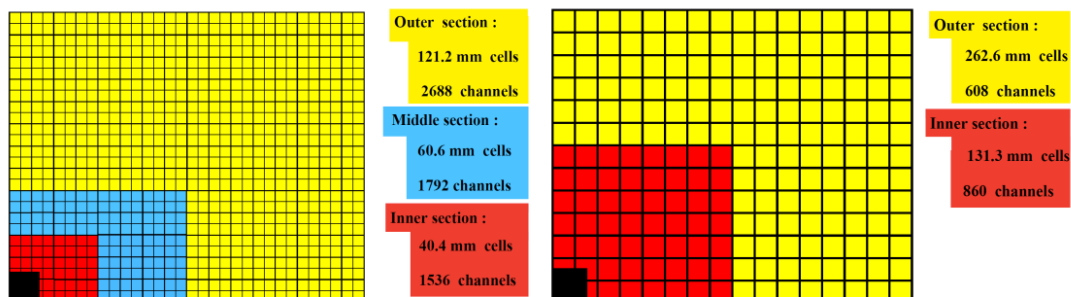


**Figure 2.7:** Lateral segmentation of (left) the ECAL and (right) the HCAL. One quarter of the detector front face is shown [7].

### 2.4.3 Muon Detectors

The LHCb muon detector is composed of four stations M2-M5 consisting of 1104 multi-wire proportional chambers (MPWC) for a total area of 385 m<sup>2</sup>, all located downstream the calorimeter system. During Run 1 and 2, an additional chamber M1 comprising both electron multiplier (GEM)s and MPWCs was installed upstream the calorimeters. Its main purpose was to provide information for the hardware L0 trigger and it has thus been removed in Run 3. Each station is composed of two independent halves, Side A and Side C. The four stations are equipped with MPWCs and interleaved with 80 cm thick iron absorbers to filter low energy particles. Each station is divided into four regions, whose area and segmentation scale in order to uniformly distribute the particle flux and the channel occupancy across each station. The MWPCs are made of four independent layers, each consisting of anode wires between cathode planes for high efficiency.

## Chapter 3

# The PLUME detector

Luminosity levelling, *i.e.* keeping the instantaneous luminosity stable within a  $\pm 5\%$  range, is vital to preserve the LHCb sub-detectors integrity and a good data quality. During Run 1 and 2, the real-time luminosity was inferred from the activity in the LHCb calorimeter, and it was then used in the hardware L0 trigger, no longer present in Run 3. The purpose of the Probe for LUMinosity MEasurement (PLUME) is to monitor the instantaneous luminosity, both with online measurements (performed per bunch) and offline data analysis. Moreover, PLUME is deployed to measure radiation background and the level of ghost charges alongside the Radiation Monitoring System (RMS) and the Beam Condition Monitor (BCM). A brief overview of the PLUME detector follows.

### 3.1 PLUME detector layout

The two-layer PLUME hodoscope is composed by 48 elementary modules arranged in a projective geometry, with a cross shape around the beam tube. The layout can be seen in Figure 3.1. The detector box is mechanically protected by an outside grid, common to VELO, SMOG2 and PLUME detectors.

Both PLUME layers host 24 modules. The first layer of PMTs is located at 1680 mm from the nominal interaction point, while the second one is positioned at 1900 mm. The alignment in  $x$  and  $y$  has an accuracy below 1 mm, while the alignment in  $z$  is less constraining due to the significant extension of the luminous region along the beam line. The modules are positioned at angles in the range of  $5^\circ - 10^\circ$  with respect to the beam axis as shown in Figure 3.2.

The integration of PLUME takes into account the neighbouring systems VELO, SMOG2 and BCM and their infrastructures, as well as the beam pipe and the vacuum system.

### 3.2 Elementary detection module

The PLUME detector exploits the Cherenkov light produced in quartz material by particles coming from the collision region. The 48 elementary detectors constituting the two-layer hodoscope of PLUME are photomultiplier tubes (PMTs) with quartz entrance windows and an additional optically connected 5 mm thick quartz tablet. A schematic view of the module is displayed in Figure 3.3. The PMT and the divider circuit are

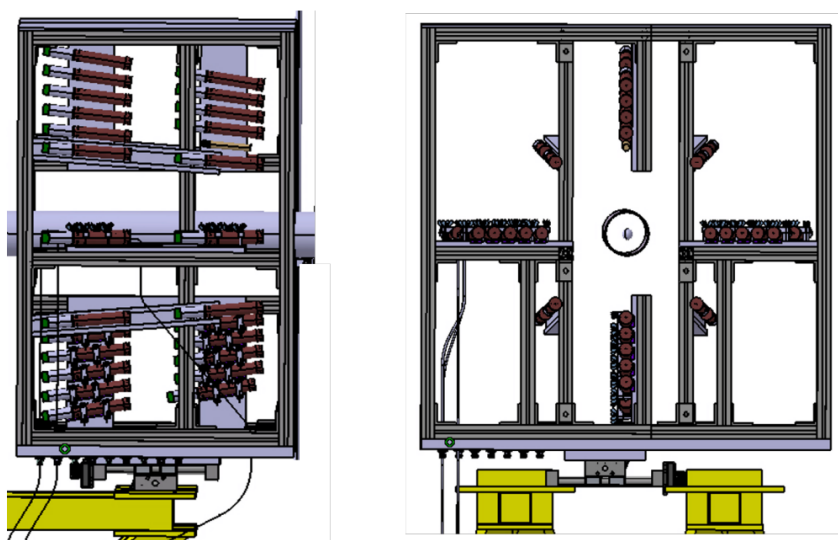


**Figure 3.1:** PLUME detector arrangement, (left) side and (right) beam views. Cable and fiber routing for one elementary detector module is shown [5].

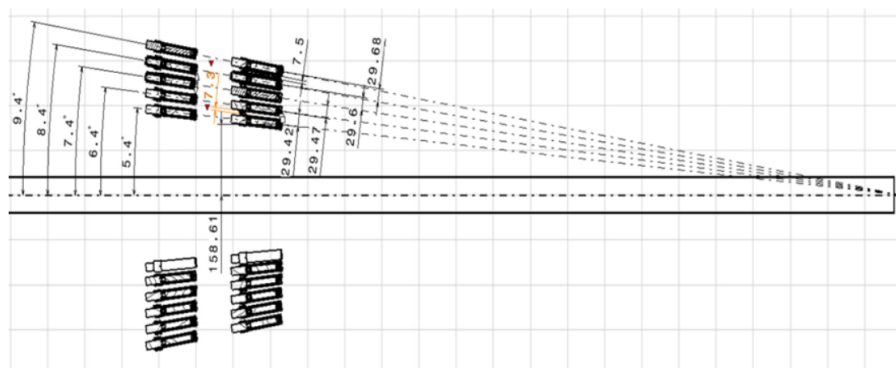


**Figure 3.2:** Angular positions of PLUME elementary detectors with respect to the nominal primary  $pp$  collision vertex [5].

fit inside an aluminium cylindrical shield that protrudes beyond the window to host the quartz tablet and the quartz fibre that brings the light to the front surface of the quartz tablet for monitoring purposes. In order to eliminate a potential effect from the remaining magnetic field, a permalloy screen surrounds the PMT.

The modules have a typical expected occupancy of around 1% and a negligible probability to get a contribution from two particles within one bunch crossing; thus a yes/no counting will be a reliable input for the *logZero* method, which will be described in chapter 4.

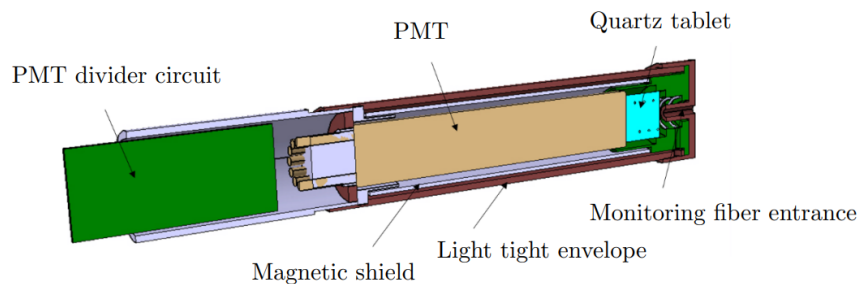


**Figure 3.3:** Schematic view of the PLUME elementary detection module [5].

### 3.3 Photomultiplier R760

The PMT chosen for PLUME is the Hamamatsu R760 PMT. The R760 is a head-on type photomultiplier tube with linear-focused dynodes structure composed by 10 steps.

This choice has been motivated by several reasons:

- the modules signal has to be within the minimum distance of 25 ns between two sequential beam crossings, to avoid spillover and for an efficient readout;
- the amount of signal from a traversing particle should be significant, so that a potential threshold drift does affect the precision of the luminosity measurement;
- the harsh environment imposes the use of radiation resistant materials (metal and quartz for PLUME).

### 3.4 Quartz radiator

The quartz tablet positioned in front of the PMT serves the purpose of increasing the amount of Cherenkov light produced by the traversing particle. The transmittance of the quartz tablet has to match the Cherenkov light spectrum range and stand the expected level of radiation: the PLUME detector employs a 5 mm thick SPECTROSIL 2000 quartz tablet, positioned in front of the 1.2 mm thick quartz PMT window.

## Chapter 4

# Measurements of PLUME effective cross-section

In this chapter, a description of the data sample and the procedure that has been adopted to measure the PLUME detector cross-section will be exposed. Three different cross-section measurements obtained by analysing three different proxies will be presented:

- **Coincidences of hits in projective PMTs**
- **Single PMT rates**
- **Average of ADC counts**

### 4.1 Data Sample

The data sample for this analysis was collected during a van der Meer scan that was performed on the 10th November 2022, starting at 07:22:14 am until 11:20:33 am. Data have been collected from different sources and detectors:

- Beams  $x$  and  $y$  positions from TIMBER, a CERN database. At every step the beams  $x$  and  $y$  coordinates may vary simultaneously or one at a time;
- Beams intensities (bunch populations) from NXCALS, a CERN database. It is important to note that the longitudinal structure of the LHC beams is shaped by the 400 MHz radio frequency (RF) system: both LHC rings are subdivided in “slots”, each containing ten RF buckets (defined by the RF system, each separated by 2.5 ns) [8]. Only one of these buckets is filled with a bunch, called the “main bunch”, while the other nine are nominally empty, resulting in a bunch separation of 25 ns. Moreover, not all slots are filled, due to the beam dump LHC system, a safety measure that requires 3  $\mu$ s to function. Nonetheless, a small fraction of the charge in a slot, typically  $10^{-3}$ , called *satellite bunches*, occupies nominally empty buckets. Nominally empty slots may contain charges as well, the so called *ghost-charge*. To determine the population of the main bunches, different devices are deployed. The circulating beam current is measured non-destructively by current transformers, that exploit the measurement of the beam’s magnetic field. These devices do not

depend on the beam energy and have low detection threshold. There are two types of devices used for this measurement:

1. FBCT (Fast Beam Current Transformers): fast measurement of charge sharing among bunches. It furnishes a relative measurement of charge, that is the charge owned by every bunch. Currently there are two devices per beam that are designed to produce a signal proportional to the charge in each 25 ns LHC bunch slot. The small ghost charges in not nominal bunches are below threshold, therefore they are not detected. The FBCT cross-section systematic uncertainty is well below 1%, therefore negligible;
2. DCCT (DC Current Transformers): four independent devices, two per ring, measuring the total beam current circulating in the LHC ring. The DCCT is designed to be insensitive to the time structure of the beam, providing very precise but slow measures. Ghost and satellite charges are counted in the total charge but produce no luminosity, so they should be subtracted from DCCT measures. Previous LHC luminosity calibration experiments showed that one of the dominant uncertainties arises from the normalization of the bunch population product  $N_1 N_2$ , but since 2011 the uncertainties are  $\leq 0.3\%$  thanks to calibration measurements and systematic studies of DCCT.

Finally, the Longitudinal Density Monitors (LDM) measure the longitudinal beam charge distribution to check for satellite charges, while at the LHCb detector the ghost-charge fraction is measured through Beam Gas Imaging (BGI), which counts beam-gas interactions in bunch-crossings. The bunch-crossings can be of four types: two colliding bunches ( $bb$ ), one beam 1 bunch with no beam 2 bunch ( $be$ ), one beam 2 with no beam 1 bunch ( $eb$ ) and nominally empty-empty bunch-crossings ( $ee$ ). BGI counts beam-gas interactions in ( $ee$ ) nominally empty-empty bunch-crossings and compares them with nominally filled bunch-crossings ( $bb$ ,  $be$ ,  $eb$ );

- PLUME data from fill 8379: the PLUME detector provides current measurements for every PMT, amounting to 44 different channels. PLUME collects data that have been selected by the Lumi Trigger (High Luminosity Trigger, HLT). The upgraded trigger comprises two levels, HLT1 and HLT2 [9]. The trigger is random and, therefore, unbiased. The HLT1 level runs at a 30 MHz rate, corresponding to the rate of proton-proton collisions in LHCb. The HLT1 is the first trigger stage and performs partial event reconstruction to reduce the data rate by a factor of 30. The data are then passed to a buffer-system that allows real-time calibration and alignment of the detector. With these data, HLT2 carries out the full and improved event reconstruction [10].

In this analysis, only  $bb$  crossings have been taken into account, neglecting the  $eb$  and  $be$  background.

For the analysis, the PLUME data have been time-aligned with the data from TIMBER and NXCALS using Epoch time. The Unix Epoch (or Unix time) is the number of seconds that have elapsed since 00:00:00 UTC on 1 January 1970, not counting leap seconds. Even though Epoch literally is Unix time 0, it is commonly used as a synonym for Unix time.

All TIMBER, NXCALS and PLUME data have been subdivided according to the van der Meer steps, in order to get a  $\mu$  value for each step.

The analysis has been carried out only for the first phase of the van der Meer scan, from 07:22:14 am until 07:53:44 am, as can be seen in Figure 4.1. The picture also shows that this part consists of two one-dimensional van der Meer scans: this means that only one coordinate, the same for both beams, changed at each step while the other stayed fixed. Both scans consisted of 42 steps. The first one-dimensional scan (from the start until 07:36:49 am) was performed over  $x$  at fixed  $\Delta y_0 \simeq 0.215$  mm, while the other one (from 07:38:16 am until 07:53:44 am) was performed over  $y$  at fixed  $\Delta x_0 \simeq 0.026$  mm.

## 4.2 Data Analysis

The main goal of this analysis was to determine the value of the PLUME detector effective cross section in three different cases. This section will describe the two fundamental parts of which the analysis is composed: the first one consists of a maximum-likelihood fit to the data using a Gaussian function with a linear background that was performed on the number of visible interactions obtained for every van der Meer scan step, in all three cases. This quantity can be obtained via the so-called *logZero* method, described in the next section. The second part of the analysis is the computation of the cross-section uncertainty, both via classical propagation of uncertainties of correlated quantities and a toy Monte Carlo generation.

### 4.2.1 The LogZero Method

Recalling chapter 1, the integral in Equation 1.24 can be performed once the number of visible interactions per bunch crossing is known:  $\mu$  can be computed via the so called *logZero* method, assuming Poisson statistics [5]. The probability of having  $\mu$  interactions over  $n$  events is given by

$$P(n) = \frac{\mu^n}{n!} e^{-\mu}, \quad (4.1)$$

leading to

$$\mu = -\log P_0 = -\log \frac{N_0}{N} - \frac{1}{2} \left( \frac{1}{N_0} - \frac{1}{N} \right), \quad (4.2)$$

where  $N_0$  and  $N$  are, respectively, the number of events with no interactions (empty events) and the total number of events while  $P_0 = P(0)$  is the fraction of empty events. The second term represents a second order correction. The definition of empty event varies for every luminometer and proxy: for PLUME, empty events are the ones that produce current signals below a fixed threshold.

Equation 4.2 can be derived by assuming  $\mu$  and  $N$  fixed, while  $n_0$  follows a Binomial distribution, fluctuating around its average value  $\langle n_0 \rangle = N_0$ . Here and in the following the angular brackets indicate averaging. We know that

$$e^{-\mu} = P_0 = \frac{N_0}{N} = \frac{\langle n_0 \rangle}{N}, \quad (4.3)$$

and that, since the logarithm is non linear

$$\mu = -\log \frac{\langle n_0 \rangle}{N} \neq -\langle \log \frac{n_0}{N} \rangle. \quad (4.4)$$

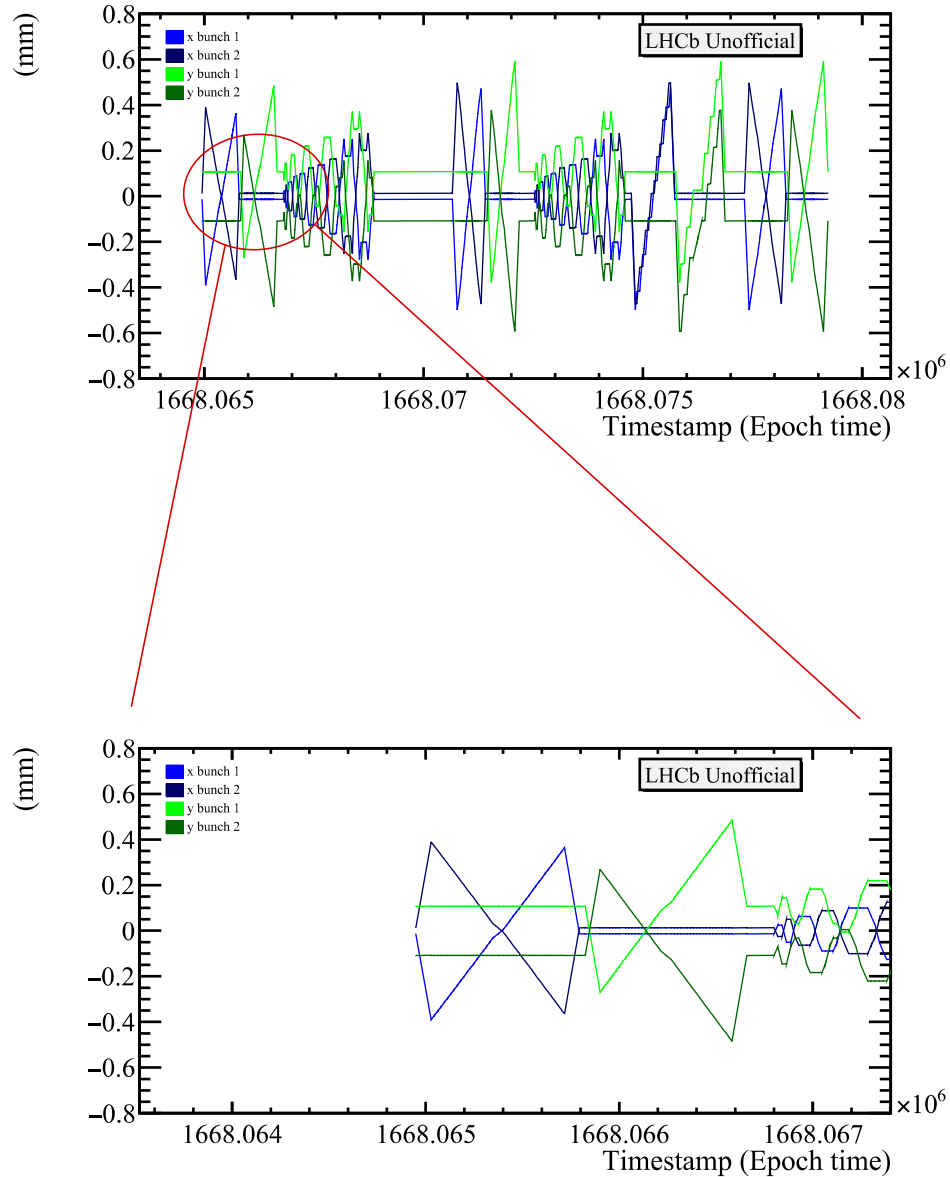


**Figure 4.1:** Beams positions during the van der Meer scan. The two figures show the complete scan (top) and the fraction that has been selected for the analysis (bottom). The blue lines refer to the beams  $x$  positions while the green ones to the  $y$  positions. The one-dimensional scan can be clearly discerned by the varying of  $x$  or  $y$  of both bunches while the other coordinate stays fixed.

The quantity  $\langle n_0 \rangle$  is unknown and only  $n_0$  is available allowing the computation of only  $\log \frac{n_0}{N}$ . In average, it approximates to  $\langle \log \frac{n_0}{N} \rangle$ , but not to  $\log \frac{\langle n_0 \rangle}{N}$ . The average bias is then equal to

$$\begin{aligned} \mu - \langle -\log \frac{n_0}{N} \rangle &= \langle \log \frac{n_0}{N_0} \rangle = \langle \log \left( 1 + \frac{n_0 - N_0}{N_0} \right) \rangle \\ &\approx \langle \frac{n_0 - N_0}{N_0} \rangle - \langle \frac{(n_0 - N_0)^2}{2N_0^2} \rangle. \end{aligned} \quad (4.5)$$

Since the revolution frequency of the LHC is 11245 Hz, the second order correction is small and thus negligible. In 3 seconds, one accumulates  $N \approx 33700$  events per bunch crossing: with a 1% occupancy ( $N - N_0 \sim 337$ ), this gives rise to a statistical uncertainty per bunch-crossing  $\sim 1/\sqrt{N - N_0} \approx 5\%$  and a statistical uncertainty for the full LHCb luminosity of  $5\%/\sqrt{n_{bb}}$ , where  $n_{bb}$  is the number of colliding bunch-bunch pairs, negligible for  $\sqrt{n_{bb}} \gg 1$ . Therefore, in 3 seconds intervals the value of  $\mu$  is stable and the deviation from Poisson statistics can be neglected.

Usually, the physics background is dominated by beam-gas interactions, that are subtracted using beam-empty ( $be$ ) and empty-beam ( $eb$ ) bunch-crossings

$$\mu = \mu_{bb} - \mu_{be} - \mu_{eb}. \quad (4.6)$$

This formula is valid only if the bunch population in the  $bb$ ,  $be$  and  $eb$  bunch crossings are similar. The beam-gas backgrounds in the  $be$  and  $eb$  bunch crossings are typically small, around 1%. Therefore the subtraction of their contribution has been neglected in the following analysis. The background in empty-empty bunch-crossings is usually negligible, but should be monitored for any anomalies.

During a van der Meer scan,  $\mu$  is measured at different displacements  $\Delta x$  and  $\Delta y$  of the colliding beams. Assuming Gaussian  $\Delta x$  and  $\Delta y$  profiles, we know that

$$\int_{-\infty}^{+\infty} C e^{-\frac{(x-\mu)^2}{2\sigma^2}} dx = C\sigma\sqrt{2\pi}, \quad (4.7)$$

so we can obtain from Equation 1.24 the expression

$$\sigma = \frac{2\pi C_x C_y \sigma_x \sigma_y}{\mu_{sp}(\Delta x_0, \Delta y_0)}. \quad (4.8)$$

In the equation above,  $\Delta x_0$  and  $\Delta y_0$  are the scan fixed points, and  $\mu_{sp}$  is the specific number of interactions, defined in chapter 1. As explained in chapter 1, these points are chosen not too far from the point of maximum luminosity, so  $\mu_{sp}(\Delta x_0, \Delta y_0)$  is, consequently, the maximum value of the specific number of interactions. The quantity  $\mu$  changes across bunches and in time and so  $N_0$  and  $N$  should be calculated per bunch in short time windows, otherwise the Poisson distribution may be biased by the  $\mu$  smearing. As said before, a 3 seconds interval is sufficient for the value of  $\mu$  to be stable.

## 4.2.2 Maximum-likelihood fit for cross-section measurements

Figure 4.2, Figure 4.3 and Figure 4.4 clearly show that the values of the number of specific interactions for each van der Meer scan step follow a Gaussian profile with a small

linear background noise, produced by beam-gas interactions. The quantities  $\sigma_x$  and  $\sigma_y$  can be defined as the beam sizes along the  $x$  and  $y$  axes, respectively. Therefore, a maximum-likelihood fit to the data has been performed, using a Gaussian function with a linear background model. Appendix A gives a more thorough explanation of the maximum-likelihood criterion. Each value of  $\mu_{sp}$  has been obtained with an average of the colliding bunches populations over the corresponding step of the van der Meer scan. On the other hand, the averages  $\langle N_1 \rangle \simeq 9.14 \times 10^{11}$ ,  $\langle N_2 \rangle \simeq 9.10 \times 10^{11}$  over all considered steps have been used for computing all cross-section measurements, as the following paragraph will show.

The resulting estimates of the Gaussian distribution maximum  $C$  and standard deviation  $\sigma$  and their respective uncertainties have been used to compute the PLUME cross-section and its uncertainty in three different ways. The main feature that distinguishes the three methods is the operational definition of the PLUME detector non-empty event.

### Cross-section with coincidences of hits in projective PMTs

Firstly,  $\mu$  has been computed by defining a non-empty event as the coincidence of hits in at least a couple of projective PMTs: this means that the signal from both PMTs, one per hodoscope layer, is above a fixed threshold.

The two performed maximum-likelihood fits are visible in Figure 4.2. The number of specific interactions  $\mu_{sp}$  is plotted against the beam displacements  $\Delta x$  or  $\Delta y$ , while the other coordinate is fixed. The plots are scaled by a factor  $10^{25}$  for improved readability, since  $\mu$  has been normalized with the product of average bunch populations to get  $\mu_{sp}$ . All the parameters that have been estimated by the fit are displayed in Table 4.1.

Parameter	Value	Parameter	Value
Background noise	$(0.22 \pm 0.04) \times 10^{-25}$	Background noise	$(0.27 \pm 0.11) \times 10^{-25}$
$C_x$	$(32.47 \pm 0.08) \times 10^{-25}$	$C_y$	$(32.3 \pm 0.3) \times 10^{-25}$
$\mu_x$ (cm)	$(-2.73 \pm 0.04) \times 10^{-28}$	$\mu_y$ (cm)	$(25.88 \pm 0.11) \times 10^{-28}$
$\sigma_x$ (cm)	$(14.35 \pm 0.05) \times 10^{-28}$	$\sigma_y$ (cm)	$(12.40 \pm 0.13) \times 10^{-28}$

**Table 4.1:** Parameters extracted from the maximum-likelihood fits visible in Figure 4.2.  $C_i$ ,  $\mu_i$ ,  $\sigma_i$  with  $i = x, y$  represent, respectively, the maximum, mean and standard deviation of the Gaussian distribution.

The cross-section has been evaluated with Equation 4.8, adjusted by a scale factor

$$\sigma = \frac{2\pi C_x C_y \sigma_x \sigma_y}{\mu(\Delta x_0, \Delta y_0)} \cdot \langle N_1 \rangle \langle N_2 \rangle \times 10^{50}, \quad (4.9)$$

where  $C_x$ ,  $C_y$ ,  $\sigma_x$ ,  $\sigma_y$  come from the fits and  $\mu(\Delta x_0, \Delta y_0) = (2.735 \pm 1.3) \times 10^{-3}$  is the maximum value of the number of interactions, not scaled with  $N_1, N_2$ . The scale factor is necessary due to the fact that  $C_x$ ,  $C_y$  have been extracted from the scaled  $\mu_{sp}$  distribution. The resulting value of the cross-section is  $\sigma = (3.57 \pm 0.04)\text{mb}$ .

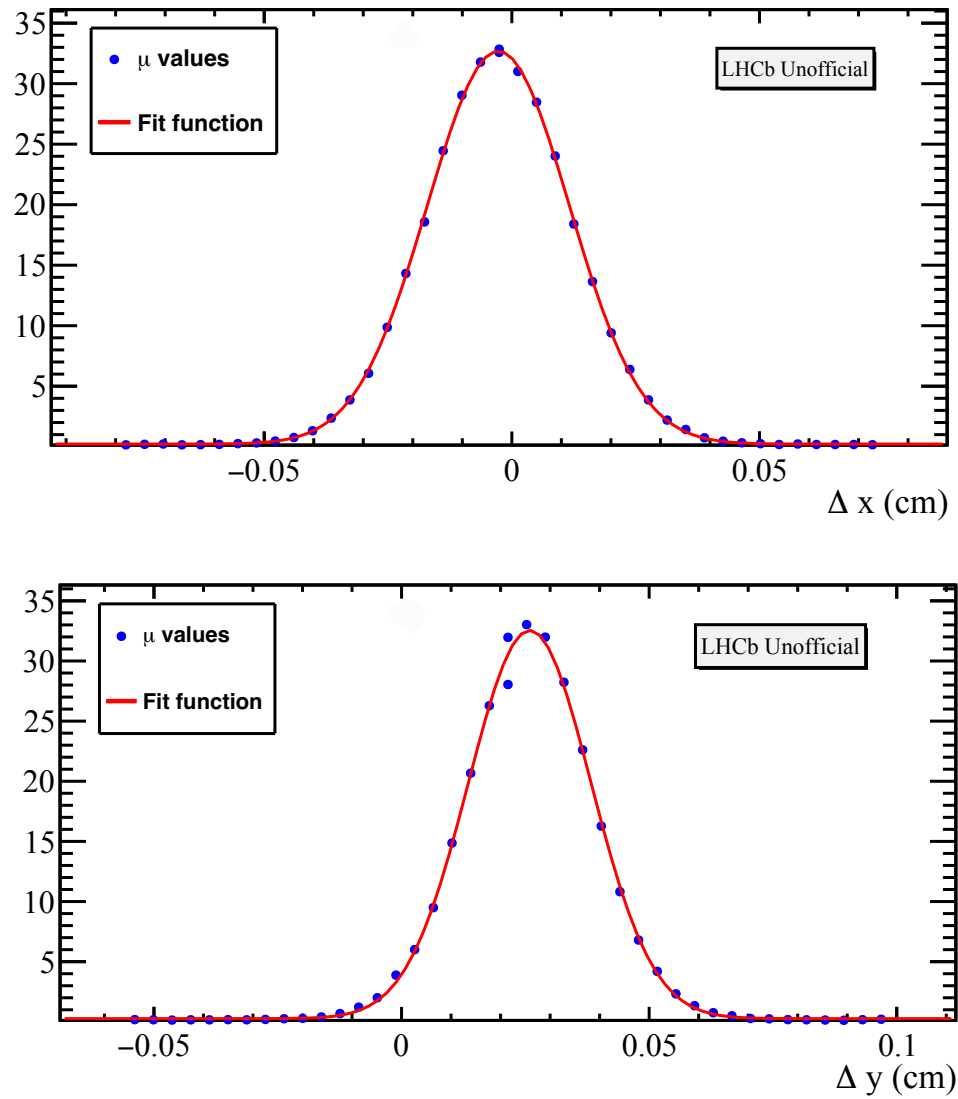


**Figure 4.2:**  $\mu_{sp}$  values (blue dots) for coincidences of hits in projective PMTs and maximum-likelihood fit projection (red line) plotted against  $x$  displacement with fixed  $\Delta y_0$  (above) and  $y$  displacement with fixed  $\Delta x_0$  (below). The Gaussian profile of  $\mu$  can be clearly seen in both plots.

### Cross-section with single PMT rates

In this case, a non-empty event has been required to have at least one signal above threshold for any PLUME PMT, *i.e.* single PMT rates.

The two performed maximum-likelihood fits are visible in Figure 4.3. As before, the number of specific interactions  $\mu_{sp}$  is plotted against the beam displacements  $\Delta x$  or  $\Delta y$ , while the other coordinate is fixed. The plots are scaled by a factor  $10^{25}$  for improved readability, since  $\mu$  has been normalized with the product of average bunch populations to get  $\mu_{sp}$ . All the parameters that have been estimated by the fit are displayed in Table 4.2.

Parameter	Value	Parameter	Value
Background noise	$(1.4 \pm 0.2) \times 10^{-25}$	Background noise	$(1.8 \pm 0.8) \times 10^{-25}$
$C_x$	$(261.9 \pm 0.5) \times 10^{-25}$	$C_y$	$(259 \pm 2) \times 10^{-25}$
$\mu_x$ (cm)	$(-2.76 \pm 0.03) \times 10^{-28}$	$\mu_y$ (cm)	$(25.84 \pm 0.11) \times 10^{-28}$
$\sigma_x$ (cm)	$(14.59 \pm 0.03) \times 10^{-28}$	$\sigma_y$ (cm)	$(12.63 \pm 0.12) \times 10^{-28}$

**Table 4.2:** Parameters extracted from the maximum-likelihood fits visible in Figure 4.3.  $C_i$ ,  $\mu_i$ ,  $\sigma_i$  with  $i = x, y$  represent, respectively, the maximum, mean and standard deviation of the Gaussian distribution.

The cross-section has been evaluated with Equation 4.8, adjusted by a scale factor

$$\sigma = \frac{2\pi C_x C_y \sigma_x \sigma_y}{\mu(\Delta x_0, \Delta y_0)} \cdot \langle N_1 \rangle \langle N_2 \rangle \times 10^{50}, \quad (4.10)$$

where  $C_x$ ,  $C_y$ ,  $\sigma_x$ ,  $\sigma_y$  come from the fits and  $\mu(\Delta x_0, \Delta y_0) = (22.1 \pm 0.4) \times 10^{-3}$  is the maximum value of the number of interactions extracted from the plot, not scaled with  $N_1$  and  $N_2$ . The scale factor is necessary due to the fact that  $C_x$ ,  $C_y$  have been extracted from the scaled  $\mu_{sp}$  distribution.

The resulting cross-section is equal to  $\sigma = (29.63 \pm 0.03)\text{mb}$ , a greater value than the one obtained with the coincidences of hits. This is predictable, since there is a less strict requirement for a non-empty event.

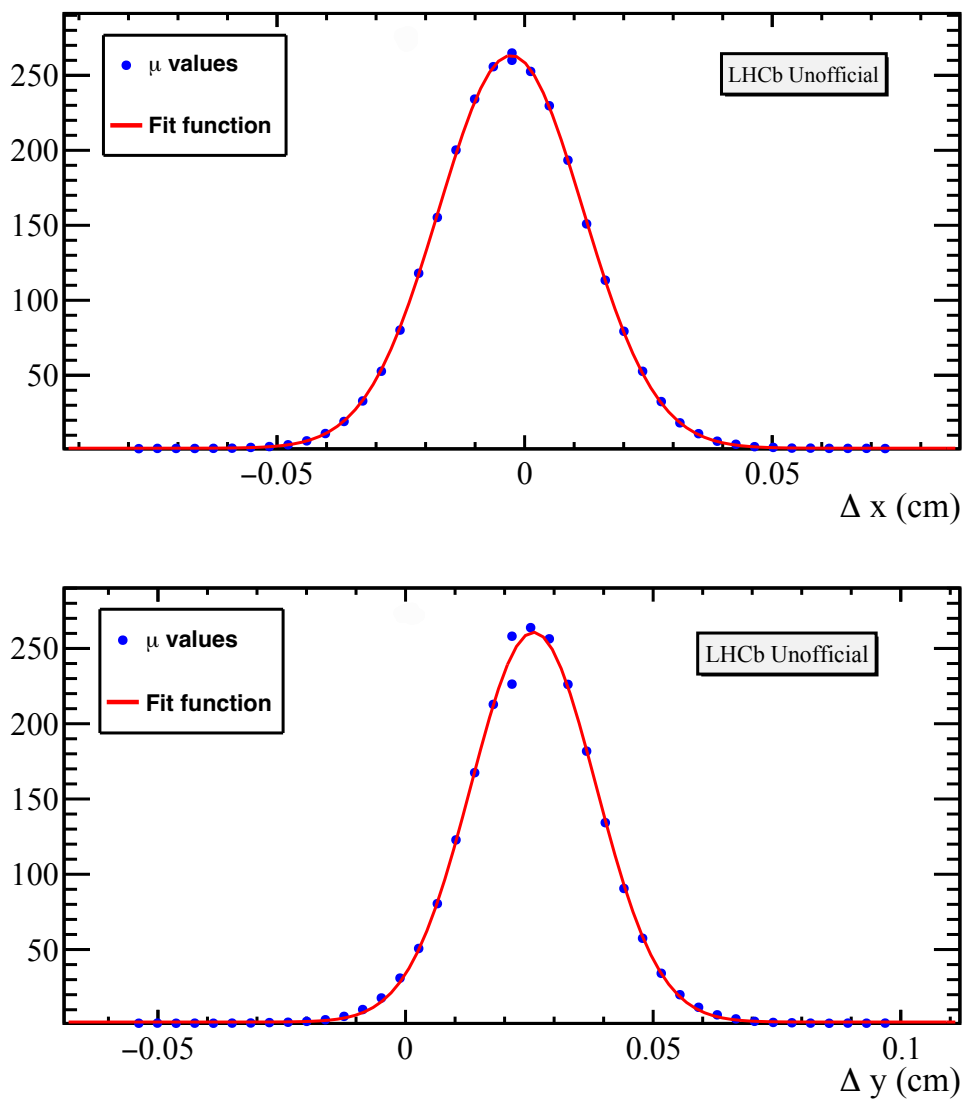


**Figure 4.3:**  $\mu_{sp}$  values (blue dots) for single PMT rates and maximum-likelihood fit (red line) plotted against  $x$  displacement with fixed  $\Delta y_0$  (above) and  $y$  displacement with fixed  $\Delta x_0$  (below). The Gaussian profile of  $\mu$  can be clearly seen in both plots.

### Cross-section with average of ADC counts

Finally, this case stands apart from the previous two since it does not involve  $\mu$  as defined in subsection 4.2.1. For every step, the corresponding quantity has been obtained instead by filling 44 different histograms, one per PMT, with the ADC signals of each PMT, and adding them all together to get another histogram. Assuming the currents from the PMTs to be independent amongst them, the mean value of the resulting histogram, divided by 44, gives the average of ADC counts. This quantity has been used in all measurements in the same way as  $\mu$ .

The two performed maximum-likelihood fits are visible in Figure 4.4. The average of ADC counts is plotted against the beam displacements  $\Delta x$  or  $\Delta y$ , while the other coordinate is fixed. The plots are scaled by a factor  $10^{25}$  for improved readability, since the ADC average has been normalized with the product of average bunch populations. All the parameters that have been estimated by the fit are displayed in Table 4.3.

Parameter	Value	Parameter	Value
Background noise	$(17.0 \pm 0.1) \times 10^{-25}$	Background noise	$(17.2 \pm 0.3) \times 10^{-25}$
$C_x$	$(103.0 \pm 0.2) \times 10^{-25}$	$C_y$	$(101.9 \pm 0.7) \times 10^{-25}$
$\mu_x$ (cm)	$(-2.70 \pm 0.03) \times 10^{-28}$	$\mu_y$ (cm)	$(25.84 \pm 0.11) \times 10^{-28}$
$\sigma_x$ (cm)	$(14.58 \pm 0.03) \times 10^{-28}$	$\sigma_y$ (cm)	$(12.60 \pm 0.12) \times 10^{-28}$

**Table 4.3:** Parameters extracted from the maximum-likelihood fits visible in Figure 4.4.  $C_i, \mu_i, \sigma_i$  with  $i = x, y$  represent, respectively, the maximum, mean and standard deviation of the Gaussian distribution.

The cross-section was evaluated with Equation 4.8, adjusted by a scale factor

$$\sigma = \frac{2\pi C_x C_y \sigma_x \sigma_y}{ADC_{mean}(\Delta x_0, \Delta y_0)} \cdot \langle N_1 \rangle \langle N_2 \rangle \times 10^{50}, \quad (4.11)$$

where  $C_x, C_y, \sigma_x, \sigma_y$  come from the fits and  $ADC_{mean}(\Delta x_0, \Delta y_0) = (10.03 \pm 0.01) \times 10^{-3}$  is the maximum value of average ADC counts, not scaled with  $N_1, N_2$ . The scale factor is necessary due to the fact that  $C_x, C_y$  have been extracted from the scaled ADC mean distribution.

The resulting value of the cross-section is  $\sigma = (10.06 \pm 0.01)\text{mb}$ . This results is in between the value of the cross section obtained with the coincidences of hits in projective PMTs and the one obtained with the average of ADC counts.

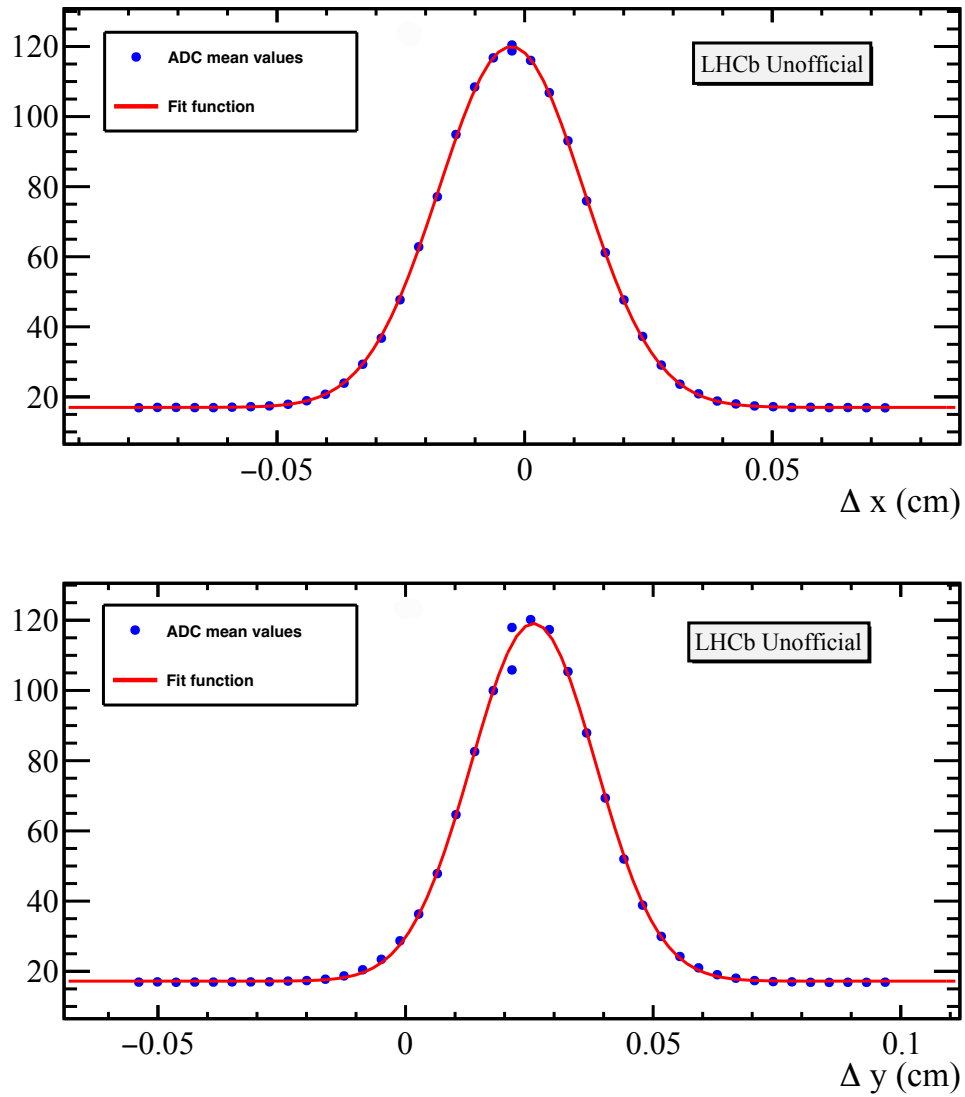


**Figure 4.4:**  $ADC_{mean}$  values (blue dots), scaled by bunches average populations and number of PMTs, and maximum-likelihood fit (red line) plotted against  $x$  displacement with fixed  $\Delta y_0$  (above) and  $y$  displacement with fixed  $\Delta x_0$  (below). The Gaussian profile of  $ADC_{mean}$  can be clearly seen in both plots.

### 4.2.3 Computation of cross-section uncertainty

The computation of the cross-section uncertainty has been performed with two different methods for each cross-section measurement. The first method is the classical propagation for non-linear correlated quantities, while the second one deals with a toy Monte Carlo random sampling.

#### Propagation of uncertainties of correlated quantities

Since the cross-section  $\sigma$  in a non linear function of its arguments, it must be linearized by an approximation to a first-order Taylor series. The uncertainty is therefore propagated as follows

$$\begin{aligned} \sigma_{\sigma}^2 \approx \sigma^2 & \left[ \left( \frac{C_x}{\sigma_{C_x}} \right)^2 + \left( \frac{\sigma_x}{\sigma_{\sigma_x}} \right)^2 + 2 \frac{\sigma_{C_x \sigma_x}}{C_x \sigma_x} + \left( \frac{C_y}{\sigma_{C_y}} \right)^2 + \left( \frac{\sigma_y}{\sigma_{\sigma_y}} \right)^2 + 2 \frac{\sigma_{C_y \sigma_y}}{C_y \sigma_y} + \right. \\ & \left. + \left( \frac{\mu}{\sigma_{\mu}} \right)^2 + \left( \frac{N_1}{\sigma_{N_1}} \right)^2 + \left( \frac{N_2}{\sigma_{N_2}} \right)^2 \right], \end{aligned} \quad (4.12)$$

where  $\sigma_{C_x \sigma_x}$  and  $\sigma_{C_y \sigma_y}$  are the covariances between  $C_x$ ,  $\sigma_x$  and  $C_y$ ,  $\sigma_y$ , respectively<sup>1</sup>. The presence of the covariance is fundamental due to the fact that the parameters  $C$  and  $\sigma$  have been extracted in the same fit and are, therefore, correlated.

The values that have been obtained with this formula are the ones that appear with the cross-section values in the previous section.

#### Propagation of uncertainties with toy Monte Carlo generation

Monte Carlo techniques are often a practical way to evaluate difficult integrals or to sample random variables governed by complicated probability density functions. The main concept is to solve deterministic problems with random generated samples.

In this analysis, the toy Monte Carlo generation has been used to cross-check the uncertainty computation described in the previous section. This approach has required the generation of Gaussian samples of each quantity involved in the cross-section measurement. The random generation has been performed with the `TRandom3` random number generator provided by the `ROOT` package. This generator implements the Mersenne twister algorithm of Matsumoto and Nishimura, characterised by an extremely long period of  $2^{19937} - 1$ . Each parameter was extracted multiple times according to a generated Gaussian distribution whose average and width were equal to, respectively, the parameter's original value and the parameter's uncertainty, with the exception of  $C_x$ ,  $\sigma_x$ ,  $C_y$  and  $\sigma_y$ . Since  $C_i$  and  $\sigma_i$  have been extracted by the same fit, their correlation is non negligible. Therefore, the couples of parameters  $C_x$ ,  $\sigma_x$  and  $C_y$ ,  $\sigma_y$  have been generated according to a two-dimensional Gaussian distribution

$$f(x, y) = \frac{1}{2\pi\sigma_X\sigma_Y\sqrt{1-\rho^2}} e^{\left( -\frac{1}{2[1-\rho^2]} \left[ \left( \frac{x-\mu_X}{\sigma_X} \right)^2 - 2\rho \left( \frac{x-\mu_X}{\sigma_X} \right) \left( \frac{y-\mu_Y}{\sigma_Y} \right) + \left( \frac{y-\mu_Y}{\sigma_Y} \right)^2 \right] \right)}, \quad (4.13)$$

<sup>1</sup>The covariance of two quantities  $A$ ,  $B$  is defined as  $\sigma_{AB} = \rho_{AB}\sigma_A\sigma_B$ , where  $\rho_{AB}$  is the correlation between  $A$  and  $B$ .

where  $\rho$  is the correlation between  $x$  and  $y$ ,  $\mu_X, \mu_Y$  and  $\sigma_X, \sigma_Y$  are their means and standard deviations. In our case,  $x$  represents  $C$  and  $y$  represents  $\sigma$ .

For every generation, the extracted parameters have been used to compute a new cross-section value. The expected distribution of the generated cross-section values is a Gaussian distribution whose mean should be the cross-section value that has been obtained with the real data sample. Finally, the standard deviation of this distribution represents the cross-section uncertainty. Figure 4.5, Figure 4.6 and Figure 4.7 show the cross-section distributions obtained with the toy Monte Carlo method for each of the three cases studied. Table 4.4 displays the three Monte Carlo cross-section values alongside the values that have been obtained with the original data sample. The generated values are compatible with the experimental values. Moreover, the obtained uncertainties on the cross-sections are equal to the ones computed with the classical uncertainty propagation, thus giving confidence about the correctness of the procedure.

	Monte Carlo cross-section	Experimental cross-section
Coincidences of PMTs hits	$(3.55 \pm 0.04)$ mb	$(3.57 \pm 0.04)$ mb
Single PMT rates	$(29.61 \pm 0.03)$ mb	$(29.63 \pm 0.03)$ mb
Average of ADC counts	$(10.05 \pm 0.01)$ mb	$(10.06 \pm 0.01)$ mb

**Table 4.4:** Comparison of Monte Carlo generated cross-section value (left) and experimental value (right) for the three considered cases. In each case, the values are compatible.

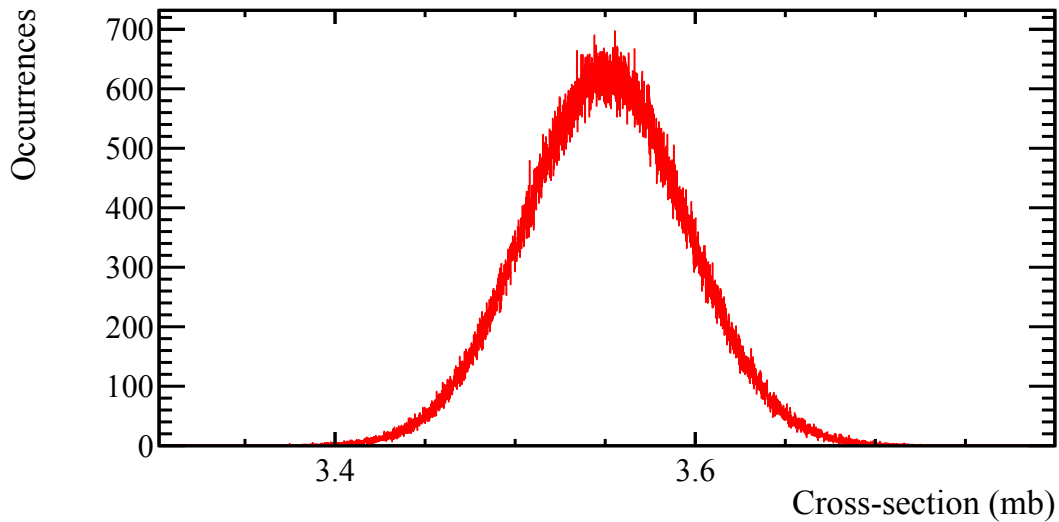


**Figure 4.5:** Monte Carlo generated cross-section for coincidences of hits in projective PMTs. The Gaussian profile is clearly visible.

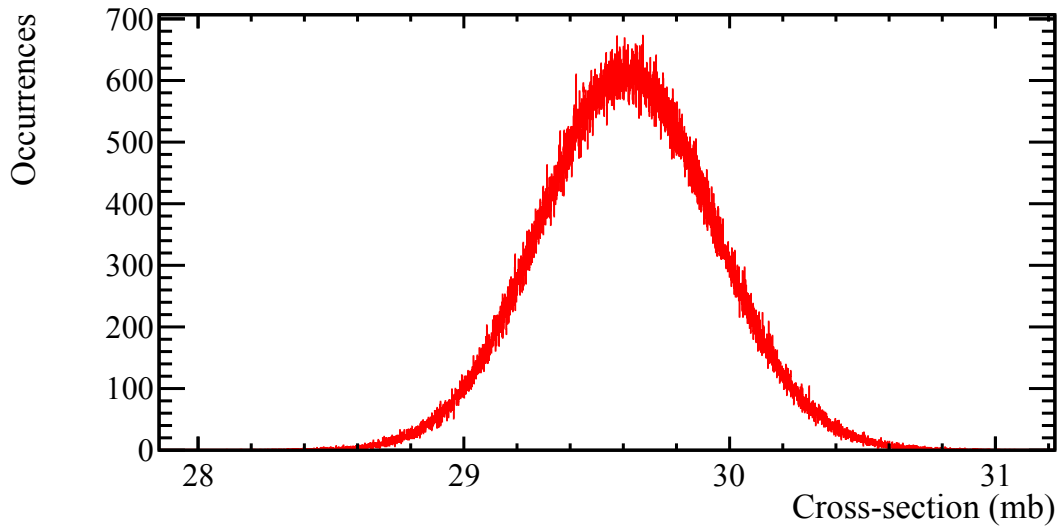


**Figure 4.6:** Monte Carlo generated cross-section for single PMT rate. The Gaussian profile is clearly visible.

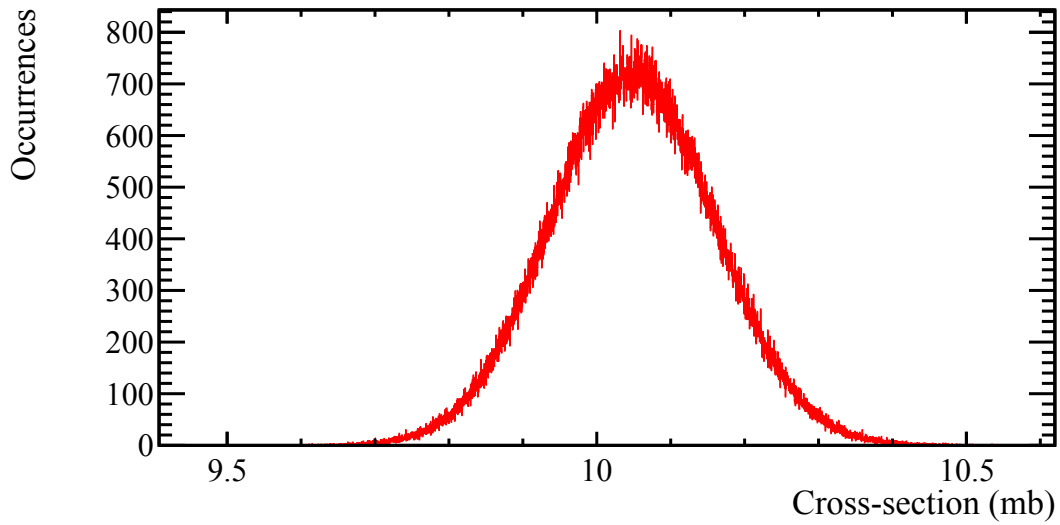


**Figure 4.7:** Monte Carlo generated cross-section for the average of ADC counts. The Gaussian profile is clearly visible.

# Conclusions

A precise knowledge of the luminosity is fundamental to ensure safe working conditions of the whole experiment and to allow precise cross-section measurements of physics processes. This thesis presents an analysis that has been performed on data collected by the PLUME detector, installed in the LHCb experiment, in order to measure its effective cross-section in three different ways. This quantity is important since it is a key ingredient needed to determine the LHCb experiment online and offline luminosity.

In order to measure the effective cross-section of a given detector one needs to know the beams width. This is obtained by the so-called van der Meer scan, that is used to measure the average number of interactions while offsetting the two beams in different directions, in order to reconstruct the beams profile. The average number of interactions can be measured exploiting the *logZero* method, that relates the number of empty and non-empty events seen by a detector to the average number of interactions. By combining the effective cross-section with the average number of interactions, the luminosity can be determined.

The three methods that have been used to compute the cross-section rely on the use of different proxies for non-empty events in the PLUME detector: coincidences of particle hits in projective PLUME elementary detectors (PMTs), a single particle hit in any PMT, *i.e.* single PMT rates, and the average of ADC counts from all the PMTs. The measured effective cross-sections are:

Coincidences of PMTs hits	$\sigma = (3.57 \pm 0.04) \text{ mb}$
Single PMT rates	$\sigma = (29.63 \pm 0.03) \text{ mb}$
Average of ADC counts	$\sigma = (10.06 \pm 0.01) \text{ mb}$

Furthermore, a toy Monte Carlo generation has been performed in order to check the cross-section statistical uncertainties, yielding the same results as the analytical uncertainty propagation. Knowing PLUME cross-section with single PMT rates and average of ADC counts will enable operation without necessarily waiting for a van der Meer scan or cross-calibration with coincidences of hits in projective PMTs in the remaining months of 2023.

# Bibliography

- [1] Werner Herr and Bruno Muratori. “Concept of luminosity”. In: (2006). DOI: [10.5170/CERN-2006-002.361](https://doi.org/10.5170/CERN-2006-002.361). URL: <https://cds.cern.ch/record/941318>.
- [2] Vladislav Balagura. “Van der Meer scan luminosity measurement and beam–beam correction”. In: *The European Physical Journal C* 81.1 (Jan. 2021). DOI: [10.1140/epjc/s10052-021-08837-y](https://doi.org/10.1140/epjc/s10052-021-08837-y). URL: <https://doi.org/10.1140%2Fepjc%2Fs10052-021-08837-y>.
- [3] Lyndon Evans and Philip Bryant. “LHC Machine”. In: *Journal of Instrumentation* 3.08 (Aug. 2008), S08001. DOI: [10.1088/1748-0221/3/08/S08001](https://doi.org/10.1088/1748-0221/3/08/S08001). URL: <https://dx.doi.org/10.1088/1748-0221/3/08/S08001>.
- [4] Ewa Lopienska. “The CERN accelerator complex, layout in 2022. Complexe des accélérateurs du CERN en janvier 2022”. In: (2022). General Photo. URL: <https://cds.cern.ch/record/2800984>.
- [5] CERN (Meyrin) LHCb Collaboration. *LHCb PLUME: Probe for Luminosity Measurement*. Tech. rep. Geneva: CERN, 2021. DOI: [10.17181/CERN.WLU0.M37F](https://doi.org/10.17181/CERN.WLU0.M37F). URL: <https://cds.cern.ch/record/2750034>.
- [6] The LHCb Collaboration et al. “The LHCb Detector at the LHC”. In: *Journal of Instrumentation* 3.08 (Aug. 2008), S08005. DOI: [10.1088/1748-0221/3/08/S08005](https://doi.org/10.1088/1748-0221/3/08/S08005). URL: <https://dx.doi.org/10.1088/1748-0221/3/08/S08005>.
- [7] The LHCb Collaboration et al. *The LHCb upgrade I*. Tech. rep. 2023. arXiv: [2305.10515](https://arxiv.org/abs/2305.10515). URL: <http://cds.cern.ch/record/2859353?ln=en>.
- [8] The LHCb collaboration. “Precision luminosity measurements at LHCb”. In: *Journal of Instrumentation* 9.12 (Dec. 2014), P12005–P12005. DOI: [10.1088/1748-0221/9/12/p12005](https://doi.org/10.1088/1748-0221/9/12/p12005). URL: <https://doi.org/10.1088%2F1748-0221%2F9%2F12%2Fp12005>.
- [9] The LHCb Collaboration. “Throughput and resource usage of the LHCb upgrade HLT”. In: (2020). URL: <https://cds.cern.ch/record/2715210>.
- [10] Lukas Calefice et al. “Effect of the high-level trigger for detecting long-lived particles at LHCb”. In: *Front. Big Data* 5 (2022), p. 1008737. DOI: [10.3389/fdata.2022.1008737](https://doi.org/10.3389/fdata.2022.1008737).

# Appendix A

## The maximum likelihood method

In statistics, a given sample of data is often used to make inferences about a probabilistic model, *e.g.* to assess the model's validity or to determine the values of its parameters. The maximum-likelihood criterion allows to estimate the distribution parameters by finding the values that maximize the *likelihood function*, *i.e.* the joint probability density function for the data, evaluated with the data obtained in the experiment and regarded as a function of the parameters. This method deals with *estimators* of the parameters. An *estimator* is a function of the data whose value is intended as a meaningful guess for the value of the parameter. Maximum likelihood estimators are approximately unbiased and efficient for large data samples.

As an example, let us consider a Gaussian distribution

$$f(x) = \frac{1}{\sqrt{2\pi}\sigma} \exp\left[-\frac{(x-\mu)^2}{2\sigma^2}\right]. \quad (\text{A.1})$$

We want to find the best estimate for the parameters  $\lambda_1 = \mu$  and  $\lambda_2 = \sigma$  from a sample of  $N$  values  $x_1, x_2, \dots, x_N$ . The likelihood function that gives the probability density of obtaining the sample values  $x_1, x_2, \dots, x_N$  is the multivariate distribution

$$g(x_1, x_2, \dots, x_N; \mu, \sigma) = \frac{1}{(\sqrt{2\pi})^N \sigma^N} \exp\left[-\sum_{i=1}^N \frac{(x_i - \mu)^2}{2\sigma^2}\right], \quad (\text{A.2})$$

where  $\mu$  and  $\sigma$  are the unknowns. As said before, the estimates  $\tilde{\mu}$  and  $\tilde{\sigma}$  are the ones that maximize the multivariate density function  $g(x_1, x_2, \dots, x_N; \mu, \sigma)$ . To evaluate them, it is sufficient to impose that the partial derivatives with respect to the unknowns are zero

$$\frac{\partial g(x_1, x_2, \dots, x_N; \mu, \sigma)}{\partial \mu} = 0 \quad \frac{\partial g(x_1, x_2, \dots, x_N; \mu, \sigma)}{\partial \sigma} = 0, \quad (\text{A.3})$$

and that the second partial derivatives are negative. It can be easily verified that

$$\tilde{\mu} = \frac{1}{N} \sum_i x_i = \mu, \quad \tilde{\sigma} = \sqrt{\frac{1}{N} \sum_i (x_i - \mu)^2}, \quad (\text{A.4})$$

*i. e.* the mean and the standard deviation of the Gaussian distribution. The quantity  $\tilde{\mu}$  is an unbiased estimator of the mean, while  $\tilde{\sigma}$  is computed with the unknown parameter  $\mu$ : if  $\mu$  is substituted by its estimate, one obtains an estimator of  $\sigma$  that is consistent but not unbiased.